Numerical Dynamo Review.

Y. Ponty CNRS. G.D Cassini → Cassiopée
Observatoire de la Côte d'Azur

- Dynamo ABC
- the numeric for the experimental
  - Ponomarenko
  - G.O Roberts
  - Taylor Green - Von Kármán
- Dynamo convective (incompressible)
- New numerical method.

× inverse cascade of helicity
× quenching α effet
× Solar dynamo → S. Brun
× Geodynamo → E. Dormy

Homogeneous Dynamos and Terrestrial Magnetism

1954

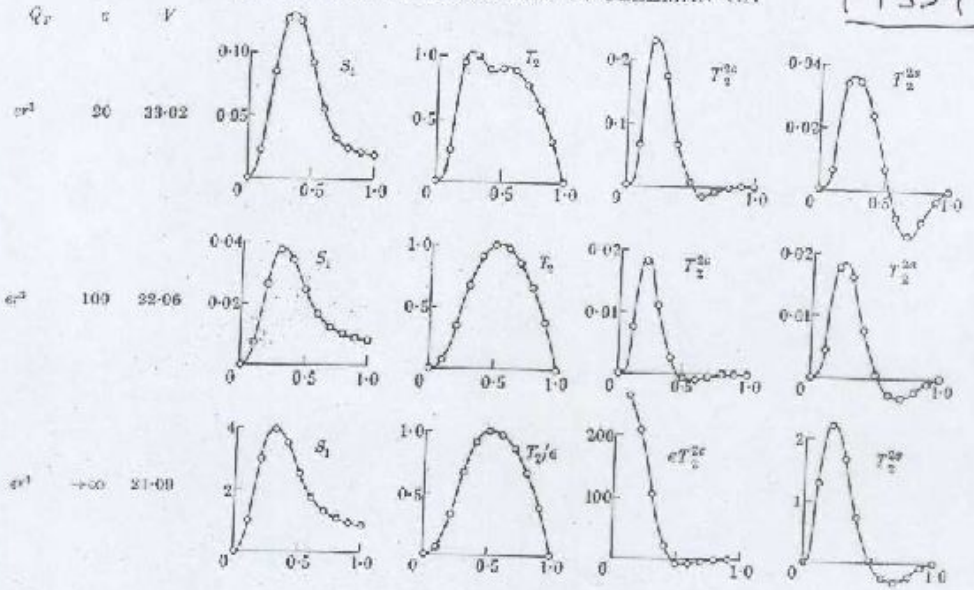

Dynamo mechanism in a rotating spherical shell: competition between magnetic field and convection vortices

NORIO ISHIHARA · SHIGEO KIDA

JFM vol 465 2002

FIGURE 9. Snapshot of magnetic and velocity fields in the first equilibrium period, seen from 30° north latitude. Contour lines of ω_r are drawn with black for positive vorticity and white for negative. The red surfaces represent $|b|$ and the grey semi-transparent ones $\omega|$.

Ecoulement ABC

T. DOMBRE, U. FRISCH, J.M Greene, M. HÉNON
A. MEHR and A.M Soward.
"Chaotic Streamline in the ABC flows"
J. Fluid Mech (1986) vol 167, pp. 353-391.

Arnold Beltrami Childress (ABC)

$$u = \begin{bmatrix} A \sin z + C \cos y \\ B \sin x + A \cos z \\ C \sin y + B \cos x \end{bmatrix}$$

Beltrami flow $\Rightarrow$ $\omega = \nabla \times u = u$

Kinematic Dynamo Childress (1967, 1970), Robert 197

3 helical waves $\Rightarrow$ natural candidate for α effect Dynamo

$A = B = C \Rightarrow$ Symmetries $\Rightarrow$ Stagnation point !

α - point unstable - stable - stable manifold

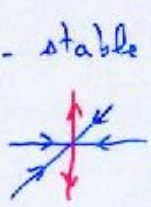

β - point unstable - unstable - stable manifolds

JFM Vol 167 (1986)

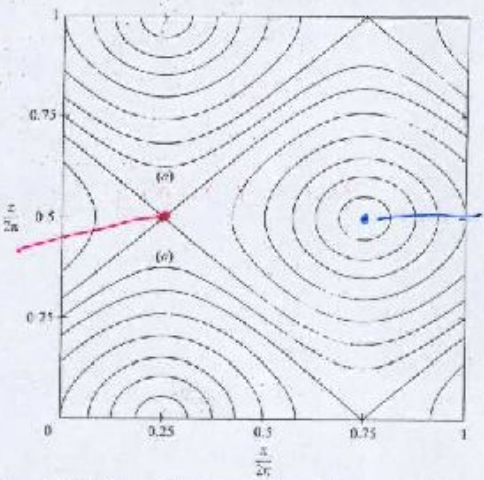

FIGURE 3. The integrable case: projection of streamlines on (x, y)-plane.

Chaotic streamlines in the ABC flows

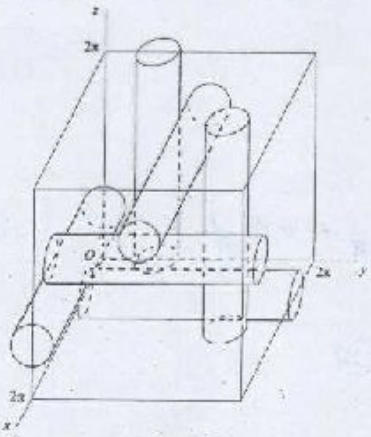

FIGURE 4. Sketch of the six principal vortices.

JFM vol 167 (1986)

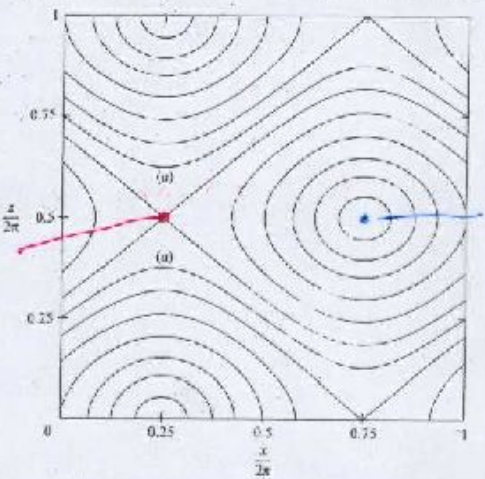

FIGURE 3. The integrable case: projection of streamlines on (x, z)-plane.

Chaotic streamlines in the ABC flows

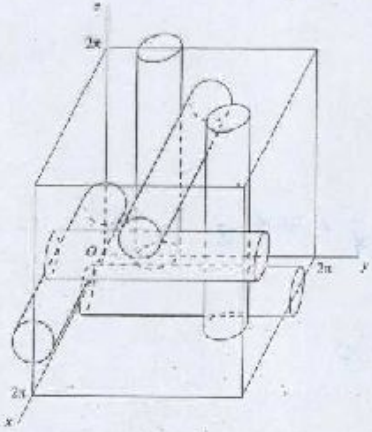

FIGURE 4. Sketch of the six principal vortices.

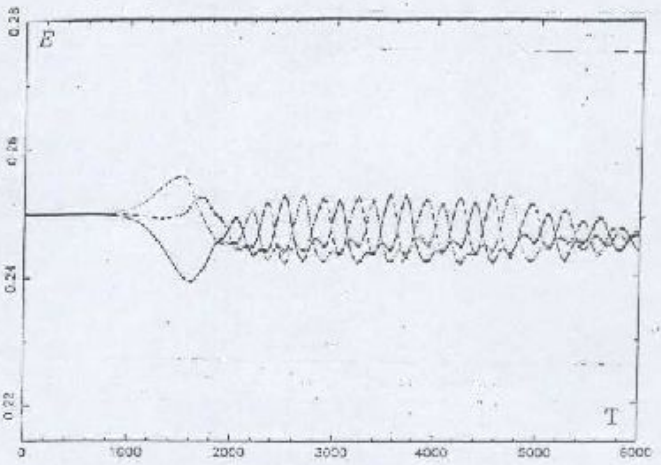

Figure 1. Evolution of the energy of the basic modes of the $\mathcal{A}_1$ flow for $\epsilon = 0.115$ ($R = 13.2$) in the doubly periodic regime. Solid line: mode (100); dashed line: (010); dotted line: (001).

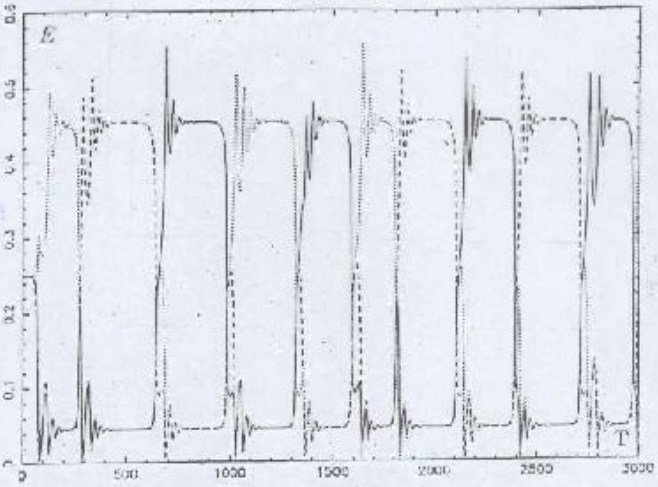

Figure 3. Evolution of the energy of the basic modes of $\mathcal{A}_1$ for $\epsilon = 0.53$ ($R = 20$). Note the emergence of two other flows, symmetric to $\mathcal{A}_1(\epsilon)$

P. Ashwin . O. Podvigina. "Hopf bifurcation with ..... Abelian
Proceedings A of the Royal Society

Slow and Fast Dynamos

$$\partial_t \mathrm{B} = \nabla \times (\mathrm{u} \times \mathrm{B}) + \epsilon \nabla^2 \mathrm{B} \qquad Rm = \varepsilon^{-1}$$

$$\mathrm{B} = e^{\sigma(\epsilon)t}\mathrm{b}$$

$$\gamma(\epsilon) = \sup_i \mathcal{R}(\sigma_i(\epsilon))$$

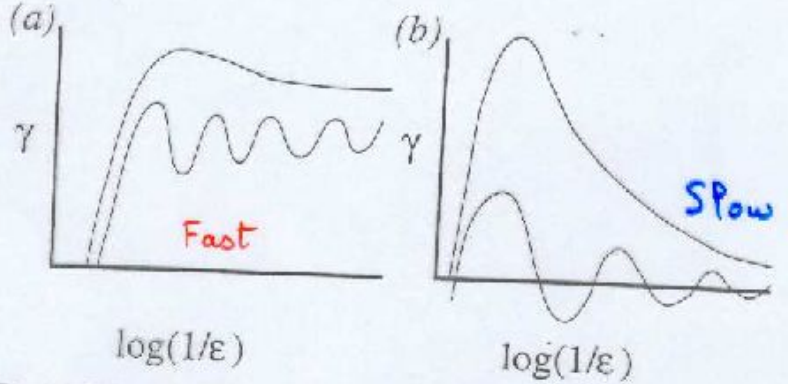

Fig. 1.2 Schematic picture of possible growth rates for fast and slow dynamos: $\gamma(\epsilon)$ against $\log R = \log(1/\epsilon)$ for (a) fast dynamos, and (b) slow dynamos.

Table 1.1 Magnetic Reynolds numbers in astrophysics.

Object	L (m)	U (m/s)	η (m^2/s)[a]	τ_T (s)[b]	R	ε^{-1}
Core of Earth	10^6	10^{-3}	1	10^{12}	10^3	
Core of Jupiter	10^7	10^{-1}	1	10^{14}	10^6	
Solar conv. zone	10^6	10^3	10^3	10^9	10^8	
Solar corona	10^9	10^3	1	10^9	10^{12}	
Interstellar medium[c]	10^{17}	10^3	10^3	10^{17}	10^{17}	
Galaxy[c]	10^{18}	10^4	10^3	10^{17}	10^{19}	

[a] Molecular value.
[b] Using η_T such that $R_T = 10^3$.
[c] Average value. Values of R are dramatically reduced when R is based on ambipolar diffusion, a dynamical effect; in this case Zeldovich *et al.* (1983) cite $R \sim 10^6$ in galaxies.

1.4 Stretch–Twist–Fold: the STF Picture

The distinction between slow and fast dynamos was first drawn by Vainshtein & Zeldovich (1972) in a paper on astrophysical magnetic fields. In this paper they describe the 'rope' or stretch–twist–fold (STF) fast dynamo, which is the archetype of the elementary models of the process. We show it in Fig. 1.3.

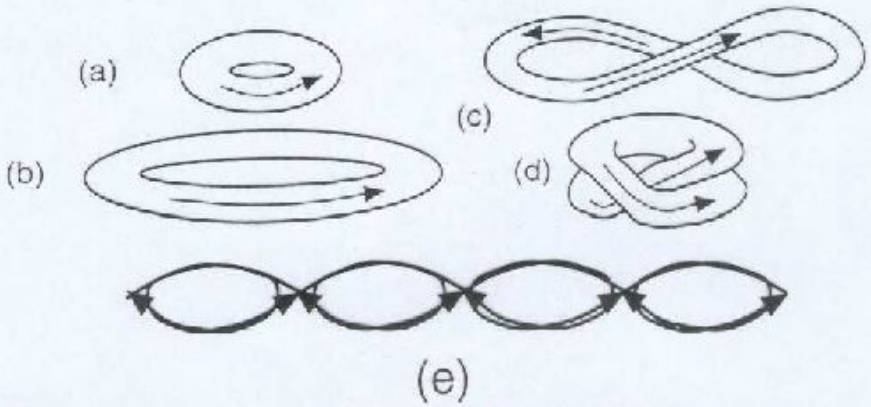

Fig. 1.3 The stretch–twist–fold (STF) fast dynamo. A torus (*a*) carrying magnetic flux F is stretched to twice its length (*b*), then twisted to give (*c*), and finally folded to give (*d*). The process preserves orientation, thus yielding a torus of roughly the original shape, but now carrying flux $2F$. (*e*) The process applied to an array of identical tori. We show the result of the stretch–twist as in (*c*) applied to a one-dimensional array of tori, resulting in flux doubling of every torus.

Measures of Stretching

- *Liapunov exponent*
- *line-stretching exponent*

Measures of the folding

- *Cancelation exponent*

D. Galloway and U. Frisch

"Dynamo Action in a family of flows with Chaotic Streamline" GAFD vol 36

$\partial_t B = \nabla \times (v \times B) + R_m^{-1} \Delta B$ 1986

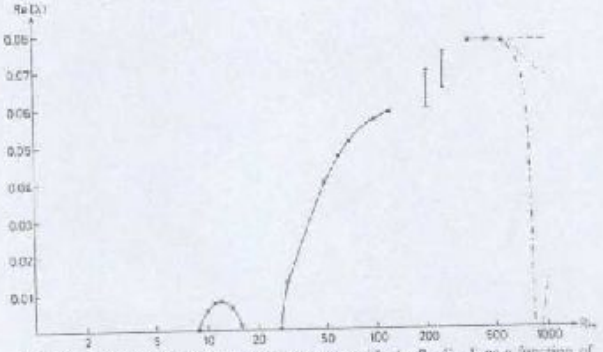

FIGURE 2. Maximum growth rate for dynamos with $A = 3$, $C = 1$, as a function of R_m. The solid line gives the numerical results; dotted lines represent conjectures on the behaviour at higher R_m.

"Spectral code"

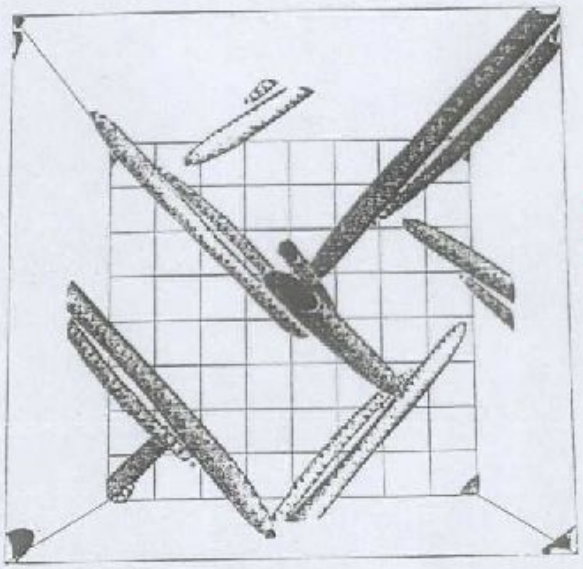

D.J Galloway and N.R O'Brian Cambridge 1992

Figure 1. Isosurface plot of the surface $|\mathbf{B}|^2 = 0.17 B^2_{max}$, for the mode in the second dynamo window with $R_m = 100$ and $A : B : C = 1 : 1 : 1$. A moment has been chosen where double cigars are clearly visible. The periodicity is apparent, and the two cigars associated with the stagnation point at $(7\pi/4, 7\pi/4, 7\pi/4)$ appear at top right.

V. Archontis , S.B.F Dorch . A. Nordlund A&A 2002

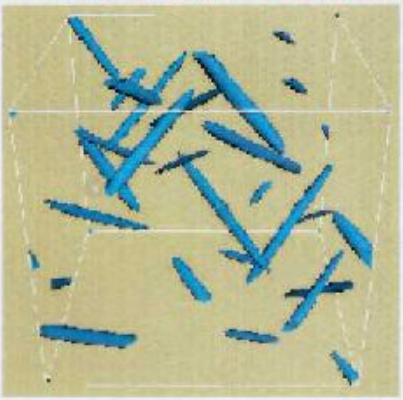

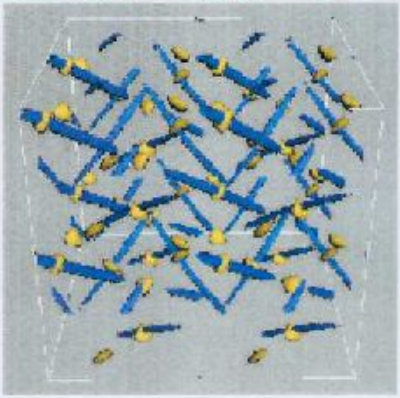

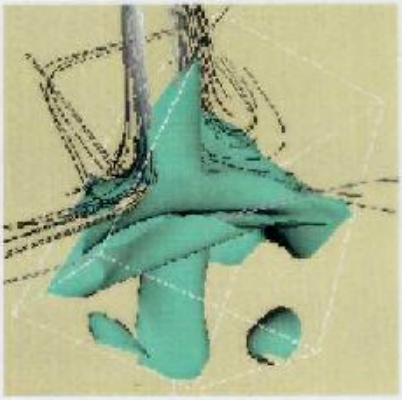

B-type

5:2:2 Four points with minimum velocity.

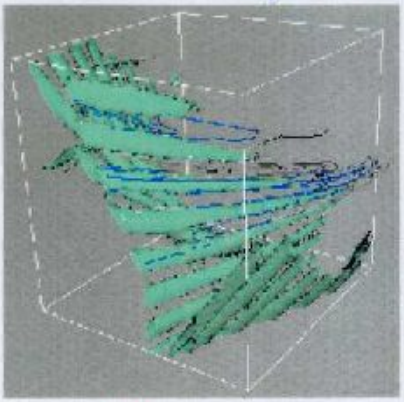

Ribbon

Plane the flow

Galloway et Proctor, Nature (1992).

L'Ecoulement ne dépend que de deux variables d'espaces ($B=0$), en lui ajoutant une perturbation temporelle.

$$u = \begin{cases} A \sin(z + \sin\Omega t) + C\cos(y + \sin\Omega t) \\ A \cos(z + \sin\Omega t) \\ C \sin(y + \cos\Omega t) \end{cases}$$

"CP flow"

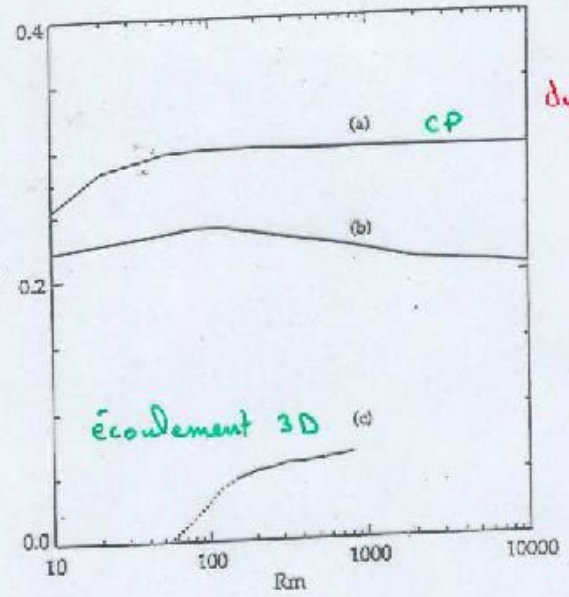

Dynamo rapide

taux de croissance de l'énergie magnétique

$A = C = \sqrt{3/2}$

$\Omega = 1$

L'équation d'induction est calculée numériquement avec un code spectral bidimensionnel.

- Mise en évidence d'une dynamo rapide.

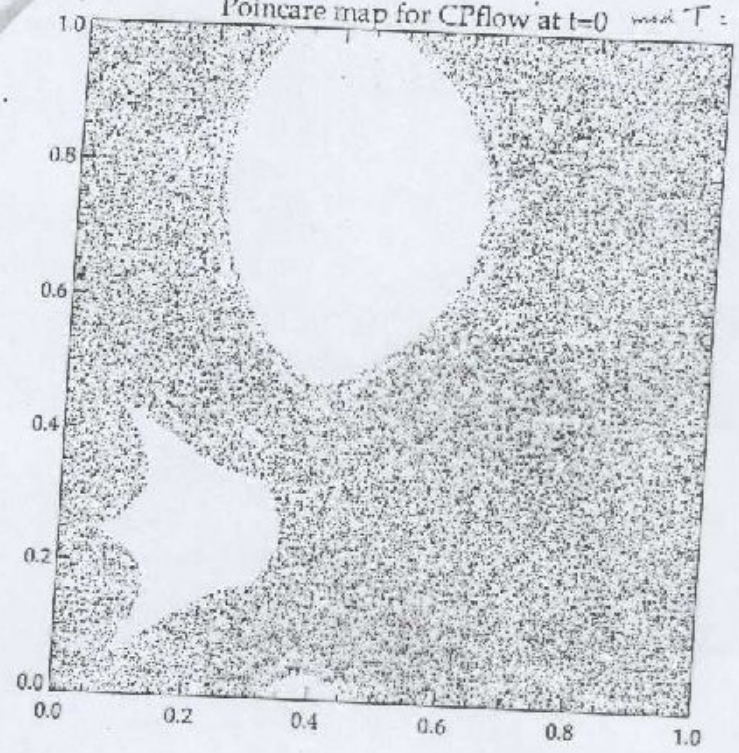
Poincare map for CPflow at t=0 and T = 2π
1.0
0.8
0.6
0.4
0.2
0.0
0.0
0.2
0.4
0.6
0.8
1.0

DYNAMO CINEMATIQUE DANS UN ECOULEMENT HAMILTONIEN FAIBLEMENT PERTURBÉ.

- PONTY, POUQUET et SULEM J. Geophys. Astrophys. Fluid Dyn. (1995)
- PONTY, POUQUET, Rom-Kedar et SULEM Theory of Solar and planetary dynamo. Cambridge Univ. Press (1993)

$$\partial_t \mathbf{b} = \nabla \times (\mathbf{u} \times \mathbf{b}) + \frac{1}{R^M} \Delta \mathbf{b}$$

$$\mathbf{u} = \begin{cases} \underline{a} \sin(z + \underline{\epsilon} \sin \underline{\omega} T) + \cos(y + \underline{\epsilon} \cos \underline{\omega} T) \\ \underline{a} \cos(z + \underline{\epsilon} \sin \underline{\omega} T) \\ \sin(y + \underline{\epsilon} \cos \underline{\omega} T) \end{cases} \quad (\underline{a}, \underline{\epsilon}, \underline{\omega})$$

$\epsilon \ll 1$

$a = 1$ hétérocline

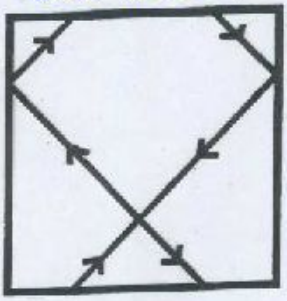

$\epsilon = 0$

$a \neq 1$ homocline

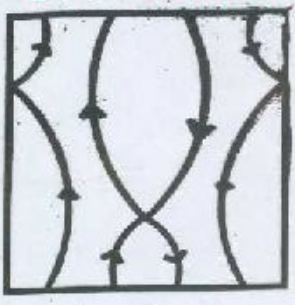

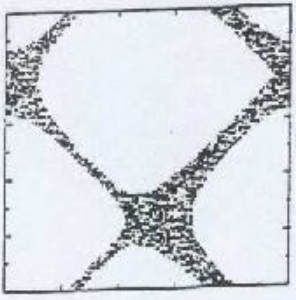

$\epsilon = 0.1$

$$\frac{dx}{dt} = u$$

• Liens quantitatifs entre l'effet dynamo
et un flot chaotique (avec A. Pouquet, P.L. Sulem).

[1] "Solar and Planetary Dynamos" Cambridge University Press, 241-248 (1993).

[2] *Geophys. Astrophys. Fluid Dyn.* **79**, 239-257 (1995).

$\|\vec{B}\|$ champ magnétique

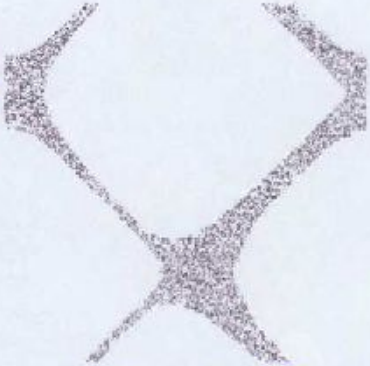

Section de Poincaré

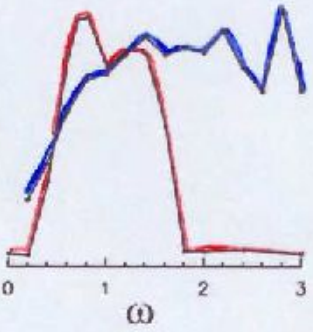

- 1er exposant de Lyapunov

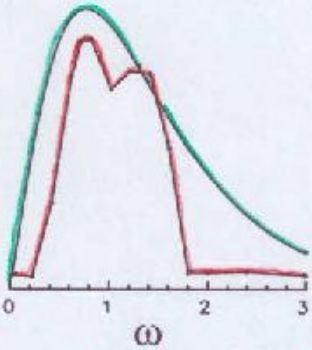

- Taux de croissance du champ magnétique

- Fonction de Melnikov estime la largeur des zones chaotiques

• Exposant de Lyapunov

• Donne le taux de séparation exponentielle de deux trajectoires initialement voisines.

• Fonction de Melnikov $F(\omega)$

• Estime la largeur des zones chaotiques

(Leonard et al. (1987), et Ollino (1989))

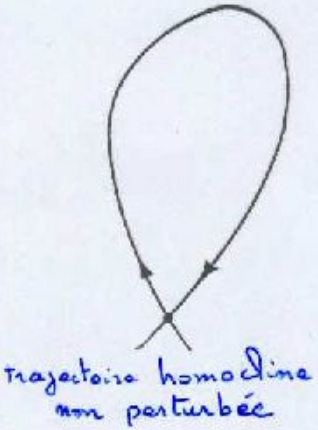

trajectoire homocline non perturbée

variétés perturbées

$$d(to) \sim \epsilon M(to) + \mathcal{O}(\epsilon^2)$$ ω fixé

• Mesure la distance entre les variétés stables et instables

$$F(\omega) = \sup_{to} M(to)$$

Prédiction du taux de croissance le plus fort suivant la fréquence ω avec la fonction de Melnikov.

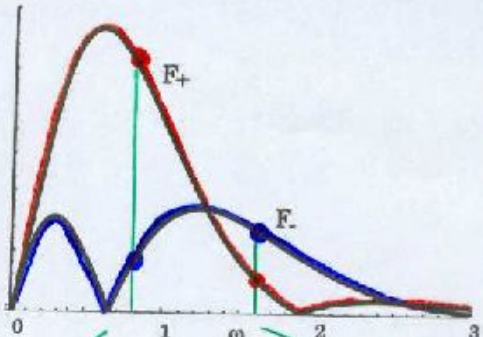

a = 0.5

ω = 0.8

ω = 1.6

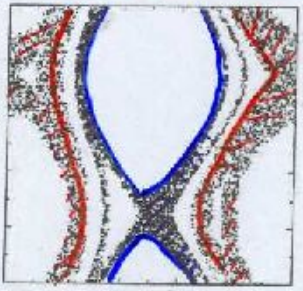

a= 0.50 ω= 0.8

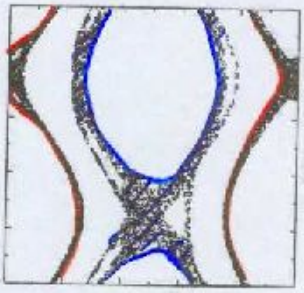

a= 0.50 ω= 1.6

$F_+ > F_-$

$F_- > F_+$

• Localisation du champ magnétique |b|

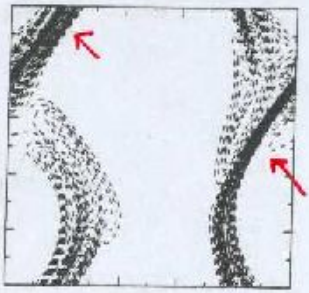

ω= 0.80

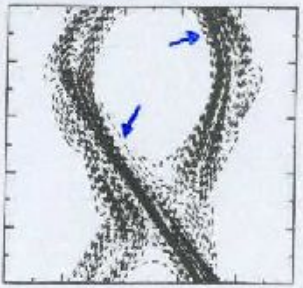

ω= 1.60

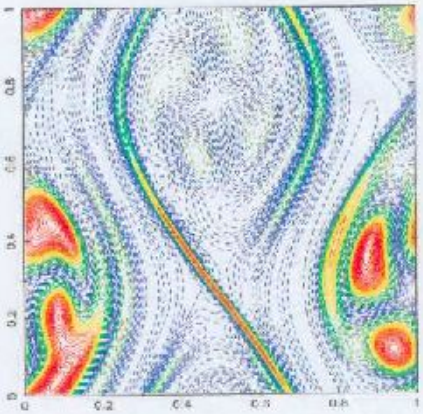
champ b
t=100.00
ε= 0.1
ω= 0.2

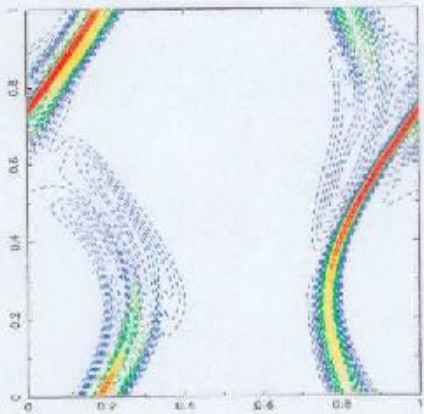
champ b
t=120.00
ε= 0.1
ω= 0.8

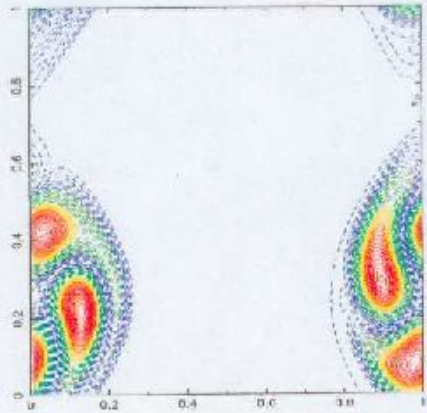
champ b
t=120.00
ε= 0.1
ω= 2.4

"Linear and Non Linear Dynamos associated with ABC flow"

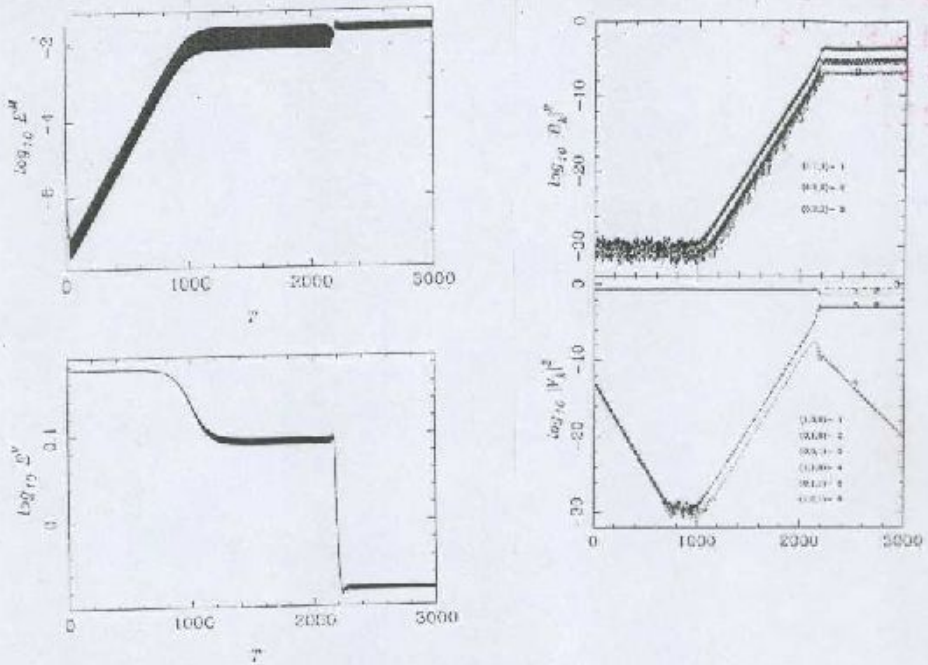

Figure 3 Time evolution of the magnetic (a) and kinetic (b) energies when the stirring force is given by equation (3.1) with $A = B = C = 1$, $k_0 = 1$, and $R^V = R^M = 12$.

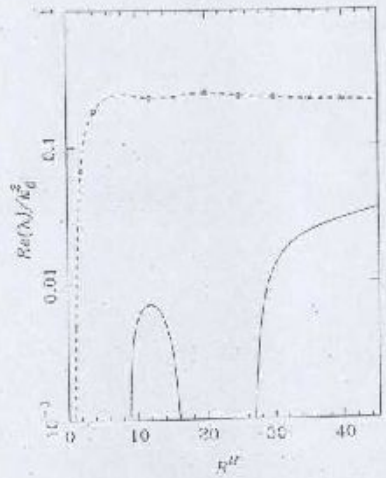

Figure 9 Growth rate of the magnetic field normalized by the rate of strain versus the magnetic Reynolds number, for the kinematic ABC dynamo with $A = B = C = 1$, for $k_0 = 1$ (solid line) and $k_0 = 7$ (dashed line).

Suppression of Chaos in a Simplified Nonlinear Model.
Fausto Cattaneo, David W. Hughes, and Eun-jin Kim
Phys. Rev. Lett
vol 76, 12
(1996).

The governing equations of MHD in dimensionless units are [6]

$$(\partial_t - R_m^{-1}\nabla^2)\mathbf{B} - \nabla \times (\mathbf{u} \times \mathbf{B}), \tag{1}$$

$$(\partial_t - R_e^{-1}\nabla^2)\mathbf{u} + \mathbf{u} \cdot \nabla \mathbf{u} = -\nabla p + \mathbf{J} \times \mathbf{B} + \mathbf{F}, \tag{2}$$

where $\mathbf{u}$, $\mathbf{B}$, and p are the velocity, magnetic field, and pressure, respectively; $\mathbf{J} = \nabla \times \mathbf{B}$ is the electric current and $\mathbf{F}$ a forcing function. The dimensionless quantities R_e and R_m are the kinetic and magnetic Reynolds numbers. By definition $\nabla \cdot \mathbf{B} = 0$ and we assume that $\nabla \cdot \mathbf{u} = 0$.

If we neglect the inertia term in the momentum equation and write

$$\mathbf{u} = \mathbf{u}_v + \mathbf{u}_I, \tag{3}$$

then (2) can be separated into

$$(\partial_t - R_e^{-1}\nabla^2)\mathbf{u}_v = -\nabla p_v + \mathbf{F}, \tag{4}$$

$$(\partial_t - R_e^{-1}\nabla^2)\mathbf{u}_I = -\nabla p_I + \mathbf{J} \times \mathbf{B}. \tag{5}$$

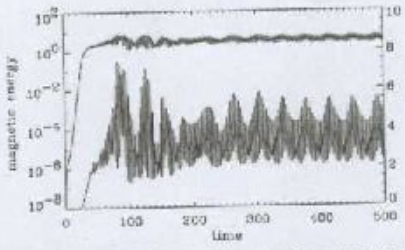

FIG. 1. Temporal evolution of the magnetic energy; $R_m = 100$. The upper curve is logarithmic (corresponding to the left-hand axis), the lower curve is linear (corresponding to the right-hand axis). The kinematic phase, during which the field grows exponentially and the backreaction is negligible, ends at $t = 30$. The saturation phase extends from $t \approx 30$ to $t \approx 250$, after which the dynamo is in its final stationary state.

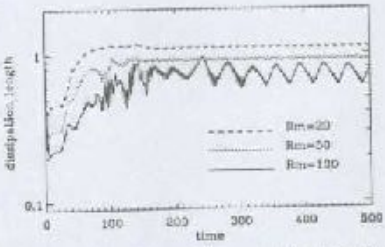

FIG. 2. Temporal evolution of the magnetic dissipation length scale for three different values of R_m.

FIG. 4. Spatial distribution of finite-time Lyapunov exponents, starting from the indicated times. The shades code the values of the exponents as a function of the initial positions. Light tones correspond to trajectories with little or no (exponential) stretching; dark tones correspond to strongly stretching trajectories. Regions of chaotic motion, which occupy a substantial fraction of the domain in the kinematic regime, are almost completely absent in the later dynamical phases.

Variable Intensity of Lagrangian Chaos in the Nonlinear Dynamo Problem.

E. Zienicke, H. Politano and A. Pouquet,

Phys. Rev. Lett. vol 81, # 21 (1998)

A dimensionalizing velocity and length scales with, respectively, A and $\ell_0/2\pi = 1/k_0$, the MHD equations write:

$$(\partial_t + \mathbf{v}\cdot\nabla)\mathbf{v} = -\nabla P + \mathbf{j}\times\mathbf{b} + (\nabla^2\mathbf{v} + \mathbf{U}^{k_0}_{111})/R^V, \quad (1)$$

$$(\partial_t + \mathbf{v}\cdot\nabla)\mathbf{b} = \mathbf{b}\cdot\nabla\mathbf{v} + \nabla^2\mathbf{b}/R^M, \quad (2)$$

where $\mathbf{v}$ is the velocity, P the pressure, $\mathbf{j} = \nabla\times\mathbf{b}$ the current density, and $\nabla\cdot\mathbf{v} = 0$, $\nabla\cdot\mathbf{b} = 0$. In the forcing term, $\mathbf{U}^{k_0}_{ABC} = (A\sin k_0 z + C\cos k_0 y, B\sin k_0 x + A\cos k_0 z, C\sin k_0 y + B\cos k_0 x)$ is a Beltrami flow ($\nabla\times\mathbf{U}^{k_0}_{ABC} = k_0\mathbf{U}^{k_0}_{ABC}$) and consists of three helical waves whose characteristic scale ℓ_0 is used to define all Reynolds numbers quoted here [16].

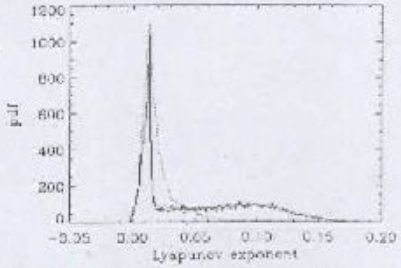

FIG. 1. Finite-time Lyapunov exponents, $R^V = R^M = 12$, $k_0 = 1$; growth (dashed line) and nonlinear (solid line) phases.

FIG. 2. Images ranging from 0 (white) to 0.25 (black) of finite-time Lyapunov exponents, $R^V = 60$, $R^M = 240$; ABC_1 flow (left), growth phase (center), and saturation (right).

"Linear and nonlinear dynamo properties of time-dependent ABC flows"

N.H Brummel, F. Cattaneo and S.M. Tobias

$$u_0 = \begin{bmatrix} \sin(z + \sin\sqrt{5}t) + \cos(y + \sin\sqrt{5}t) \\ \sin(x + \sin\sqrt{5}t) + \cos(z + \sin\sqrt{5}t) \\ \sin(y + \sin\sqrt{5}t) + \cos(x + \sin\sqrt{5}t) \end{bmatrix}$$

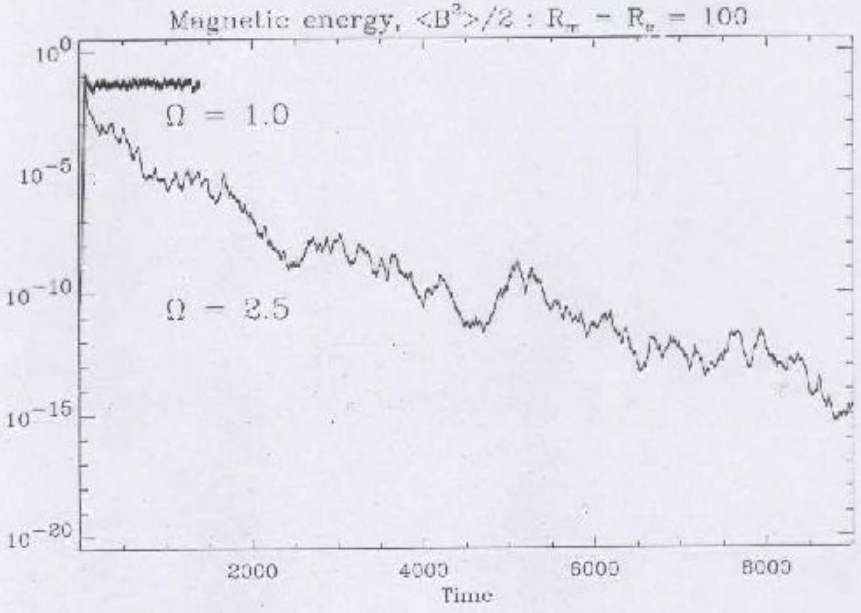

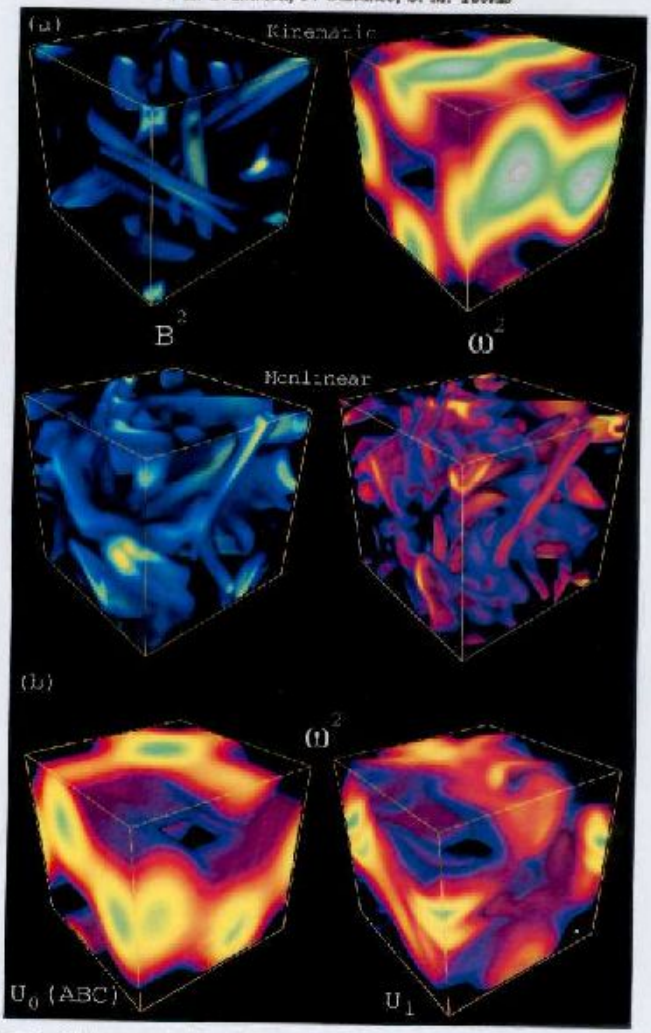

FIGURE 10. (a) Volume renderings of the magnetic energy and enstrophy densities for the typical dynamo saturation case with $\Omega = \epsilon = 1$ and $R_m = R_e = 100$. For the rendering, each value is assigned a colour and an opacity, with high values being bright and opaque (green-yellow-white) and low values being dark and translucent (black-blue-purple). The upper half of the figure shows the fields extracted from the linear regime, where the enstrophy still resembles that of the initial ABC flow $\mathbf{U}_0$ and the magnetic energy is close to that of the kinematic eigenfunction. The lower half shows a typical time in the nonlinear regime where the fields are now distinctly different from the kinematic versions. (b) Volume renderings of the enstrophy density for the flows $\mathbf{U}_0$ and $\mathbf{U}_1$ at typical times in their time-dependent evolutions. It is clear that the lengthscale for $\mathbf{U}_1$ is shorter than that for $\mathbf{U}_0$.

Ponomarenko dynamo

- Y. B Ponomarenko, J. Appl. Mech. Techn. Phys. 14. (1973)
- A.D Gilbert, GAFD 44. (1988)

Velocity Profile optimization for Riga Dynamo experiment.

F. Stephani and G. Gerbeth and A. Gailitis. (1999)

TABLE 1. Critical Rm for the considered velocity profiles

	SBR	DEF	NGB	WGB	TGB
v_z					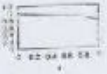
v_ϕ	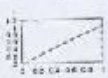		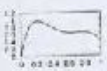		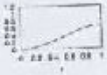
κ	1.00	1.20	0.73	1.10	1.30
Rm^*	14.9[a,b]	12.0[a,b]	25.6[b]	17.0[b]	14.3[b]
Rm^{**}	16.1[a,b]	13.2[a,b]	27.6[b]	18.3[b]	15.7[b]
Rm^{***}	16.0[a,c]	14.7[a,c]	31.0[c]	21.5[c]	17.6[c]

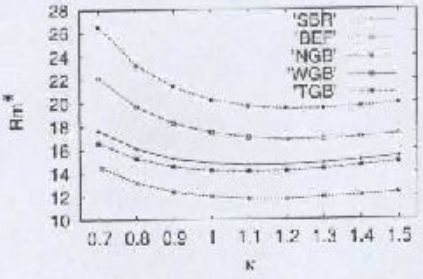

Figure 2. Dependence of Rm^* on the pitch parameter κ

Riga Results:

Gailitis et AL. Phys Rev. Lett 84 4365 (2000)
Gailitis et al Phys. Rev. lett 86. 3024 (2001)

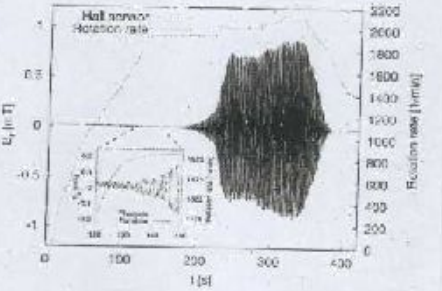

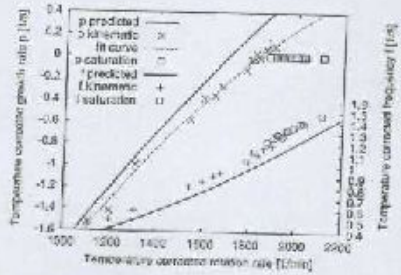

FIG. 10. Measured growth rates p and frequencies f for different rotation rates Ω in the kinematic and the saturation regime, compared with the numerical predictions. The dotted line is a fit curve for the growth rates in the kinematic regime. Ω, p, and f at the temperature T were scaled to $(\Omega_r, p_r, f_r) = \sigma(T)/\sigma(15.7\,^{\circ}\mathrm{C})\,[\Omega(T), p(T), f(T)]$ as required by the scaling properties of Eq. (4).

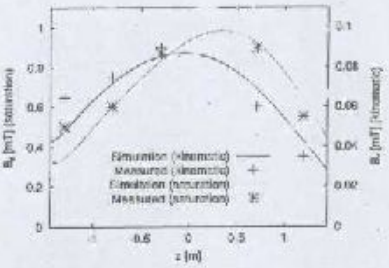

FIG. 11. Dependence of the magnetic field amplitudes on the position along the z axis of the dynamo. Measured data and predicted structure for the kinematic and the saturation regime.

Kinematic dynamo action in a network of screw motion; application to the core of fast breeder reactor.

F. Plunian, P. Marty and A. Alemany

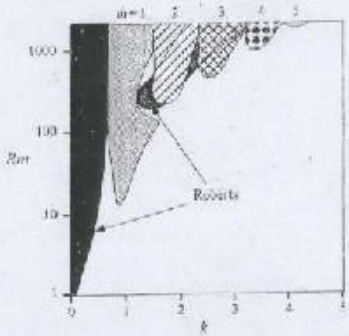

FIGURE 9. Both types of dynamo in the parameter space (k, Rm). The azimuthal mode m is indicated for the dynamo of Ponomarenko type.

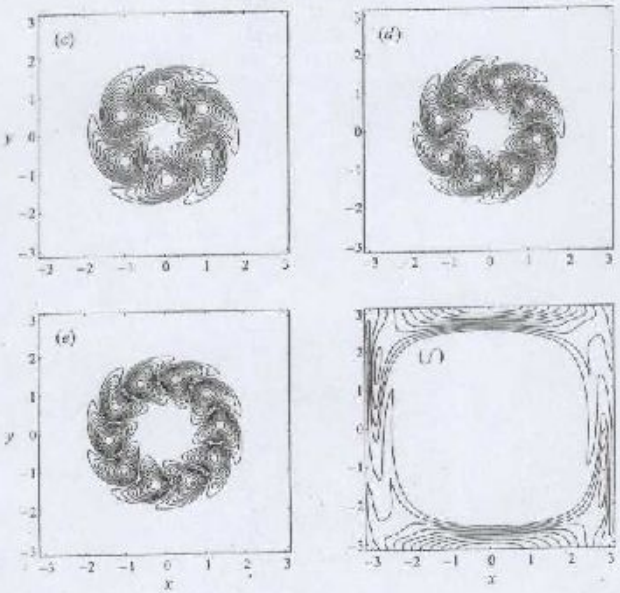

FIGURE 8. Magnetic intensity $|b|$ for $Rm = 2^{\frac{1}{2}}$ and (a) $C_{1b}k = 0.8$; (b) $C_{1a}k = 1.6$; (c) $C_{1a}k = 2.4$; (d) $C_{1b}k = 3.2$; (e) $C_{1a}k = 4$; (f) $C_{1b}k = 2.5$.

Dynamo Ponomarenko.

"Slow Ponomarenko dynamos on stream surfaces." A.D. Gilbert and Y. Ponty *Geophys. Astrophys. Fluid Dyn.* (2000).

$$\Psi = \sin x \cos \tfrac{\pi}{2} y, \quad V = \sin^2 x + y^2$$
$$y = -1 \cdots 1, \quad x = 0 \cdots 2\pi$$

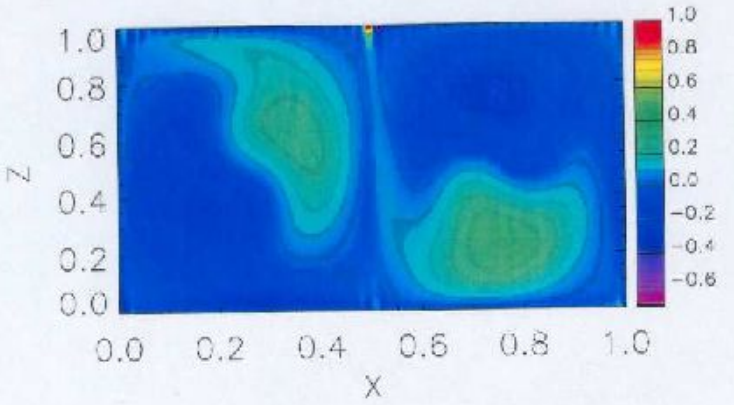

$|B|$
Magnetic field (in color)

ψ
Total velocity stream function in contour plot

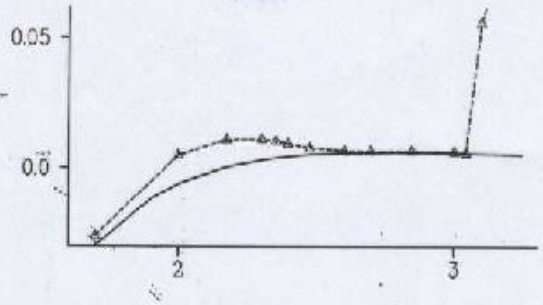

Figure 6: Growth rate p plotted against $\log_{10} R$ for the flow given by ψ, W_2, with $k = 1.5$, $m = 1$. The numerical results are shown by markers joined by a dotted line; the asymptotic results are shown by a solid line.

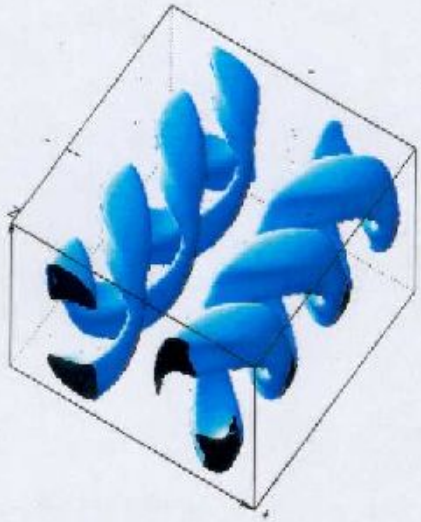

Figure 7: Growing magnetic field for the flow given by ψ, W_2, with $k = 1.5$, $m = 1$ and $R = 500$. An isosurface of constant magnetic field magnitude is shown in three dimensions.

Figure 8: Growing magnetic field for the flow given by ψ, W_2, with $k = 1.5$, $m = 1$ and $R = 2000$. An isosurface of constant magnetic field magnitude is shown in three dimensions.

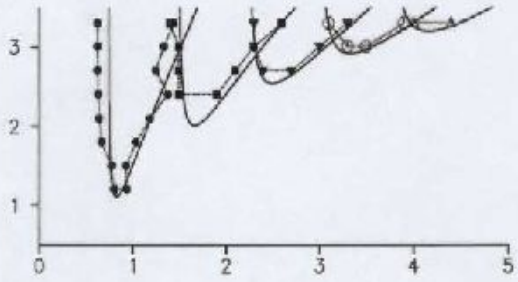

Figure 9: Comparison between the results of Plunian *et al.* (1999) and the asymptotic theory. Theoretical curves (solid) of $\log_{10} R_c$ are plotted as a function of k for $m = 1$, 2, 3, 4 and 5, reading the curves from left to right. Numerical results of Plunian *et al.* (1999) are shown by markers joined by dotted lines with $m = 1$ (solid circles), 2 (solid squares), 3 (solid triangles), 4 (open circles) and 5 (open triangles).

Nonlinear States of the Screw Dynamo

Wolfgang Dobler,* Anvar Shukurov,† and Axel Brandenburg‡
Department of Mathematics, University of Newcastle upon Tyne, NE1 7RU, U.K.
(Dated: December 14, 2002)

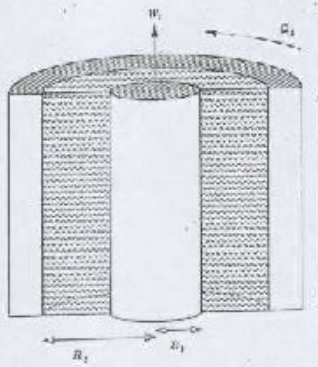

FIG. 1: Geometrical configuration of the simulations. The outer cylinder rotates at angular velocity Ω_2, while the inner cylinder moves in the axial direction at speed W_1.

Nunez et al. [30] have performed classical perturbation analysis close to the dynamo threshold for a system which is based on Ponomarenko's discontinuous dynamo model [3], but assuming the interior of the cylinder to contain fluid of fixed viscosity. For this sufficiently different system, they also find the asymptotic scaling $R_m^2 \sim \mathrm{Re}^{-1}$, while no conclusions on the asymptotic dependence on R_m can be drawn from such a model.

III. THE MODEL

A. Spiral Couette flow

The geometry of our model is shown in Fig. 1. The conducting fluid is confined in the gap $R_1 < r < R_2$ between two coaxial cylinders that move with axial velocities W_1 and W_2 and rotate with angular velocities Ω_1 and Ω_2, respectively. We choose $\Omega_1 = W_2 = 0$; the resulting flow then trivially satisfies Rayleigh's stability criterion, $\Omega_2 R_2^2 > \Omega_1 R_1^2$ [31]. The magneto-rotational instability of the Couette flow is discussed in Refs. [32, 33, 34]; our flow is stable with respect to this instability because $d\Omega/dr > 0$.

In the absence of a magnetic field, viscosity causes the fluid between the cylinders to adjust itself to the spiral Couette velocity profile

$$\Omega^{(\mathrm{C})} = C_1\left(1 - \frac{R_2^2}{r^2}\right), \qquad u_z^{(\mathrm{C})} = C_2 \ln\frac{R_2}{r}, \tag{7}$$

where

$$C_1 = \frac{\Omega_2 R_2^2}{R_2^2 - R_1^2}, \qquad C_2 = \frac{W_1}{\ln(R_2/R_1)}.$$

The velocity profile (7), driven by the viscous stress, adjusts itself over the viscous relaxation time,

$$\tau_{\mathrm{visc}} \approx \frac{(R_2 - R_1)^2}{\pi^2 \nu}. \tag{8}$$

B. Basic equations

The equations we solve are the MHD equations for the vector potential $\mathbf{A}$, the velocity $\mathbf{u}$ and the density ϱ:

$$\frac{\partial \mathbf{A}}{\partial t} = \mathbf{u}\times\mathbf{B} + \eta\Delta\mathbf{A} + (\nabla \eta)\times\mu_0\mathbf{j}, \tag{9}$$

$$\frac{D\mathbf{u}}{Dt} = -\frac{1}{\varrho}\nabla p + \frac{\mu}{\varrho}\left(\Delta\mathbf{u} + \tfrac{1}{3}\nabla\nabla\cdot\mathbf{u}\right) + \frac{\mathbf{j}\times\mathbf{B}}{\varrho}, \tag{10}$$

$$\frac{D\varrho}{Dt} = -\varrho\nabla\cdot\mathbf{u}, \tag{11}$$

complemented by an isothermal equation of state, $p = c_s^2\varrho$, with constant speed of sound c_s. Here, the magnetic flux density $\mathbf{B}$ and electric current density $\mathbf{j}$ are given by $\mathbf{B} = \nabla\times\mathbf{A}$, $\mu_0\mathbf{j} = \nabla\times\mathbf{B}$; we denote with $D/Dt = \partial/\partial t + (\mathbf{u}\cdot\nabla)$ the advective derivative; μ is the dynamical viscosity (assumed constant). Below we refer to the Reynolds number based on the average kinematic viscosity, $\nu = \mu/\bar{\varrho}$.

Equation (9) implies the gauge

$$\eta\nabla\cdot\mathbf{A} + \Phi = 0, \tag{12}$$

where Φ is the electrostatic potential, related to the electric field $\mathbf{E}$ by $\mathbf{E} = -\nabla\Phi - \partial\mathbf{A}/\partial t$. This gauge proved to be most convenient for numerical purposes. Equations (9)–(11) are written for compressible fluids, but our choice of parameters makes compressibility insignificant since the speed of sound is a factor of two larger than the maximum fluid velocity, which results in a density contrast of $\lesssim 12\%$.

We use an explicit finite difference scheme of sixth order in space and third order in time described, e.g., in Ref. [35]. The velocity field outside the fluid shell, i.e. for $r < R_1$ and $r > R_2$, is prescribed and fixed, with $\mathbf{u} = (0, 0, W_1)$ in $r < R_1$ and $\mathbf{u} = (0, \Omega_2 r, 0)$ in $r > R_2$. We embed the cylinders into a Cartesian box and solve Eqs. (9)–(11) on a Cartesian mesh in order to avoid a coordinate singularity on the axis and to retain the applicability of the code to different geometries.

The magnetic diffusivity η is assumed to be constant for $r < R_2 - 3\delta x$ (with δx the mesh size), i.e. the inner cylinder has the same electric conductivity as the fluid, but η smoothly decreases to zero in $R_2 - 3\delta x < r < R_2$. Thus, the last term in Eq. (9) is only relevant close to the outer boundary of the fluid. The outer cylinder is assumed to be magnetically impenetrable, which confines the magnetic field to the region $r < R_2$. This would best be achieved with a perfect conductor at $r \geq R_2$, but this corresponds to an infinite magnetic Reynolds

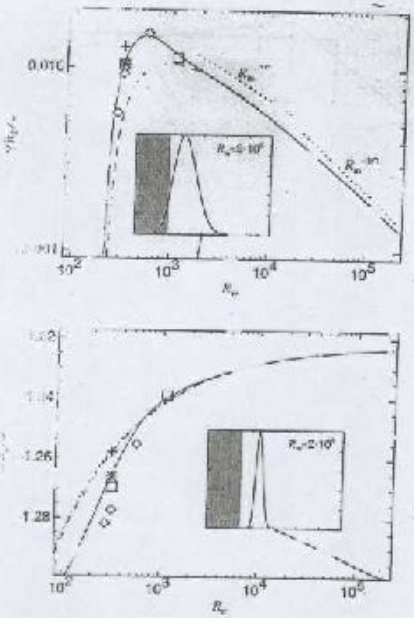

— 3: Kinematic growth rate γ and frequency ω in Model I
he mode $m = 1$, $k = k_1$ (the dominant mode) as a func-
ion of the magnetic Reynolds number, obtained from the
ree dimensional eigenvalue problem described in Sect. IV A.
Dashed lines show the dependencies $\gamma \propto R_m^{-1/3}$ and $\gamma \propto R_m^{-1/2}$
: upper panel and $(\omega - \text{const}) \propto R_m^{-1/2}$ in the lower
... The asymptotic solution given in Appendix A is shown
ashed. Results from the three-dimensional simulations are
abeled according to the grid spacing: $\delta x = 0.13$ (+), 0.087
), 0.033 (□), and 0.017 (*). The insets show radial magnetic
ne.gy profiles in the domain $0 < r < R_1$ for $R_m = 2 \times 10^3$
op), and $R_m = 2 \times 10^3$ (bottom); the region occupied by the
ner cylinder is shaded. The generation threshold for this
ird eigenmode is $R_m^{(cr)} \approx 216$.

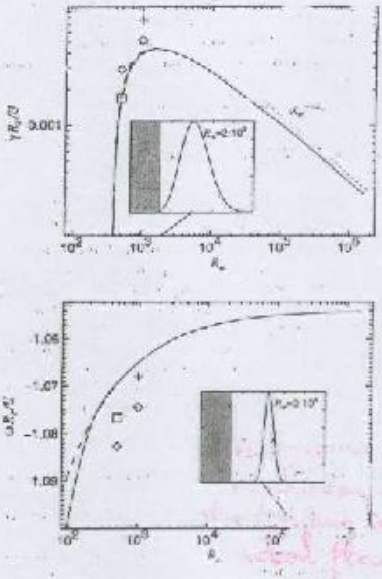

FIG. 4: As in Fig. 3, but for Mode
Reynolds number is $R_m^{(cr)} \approx 384$.

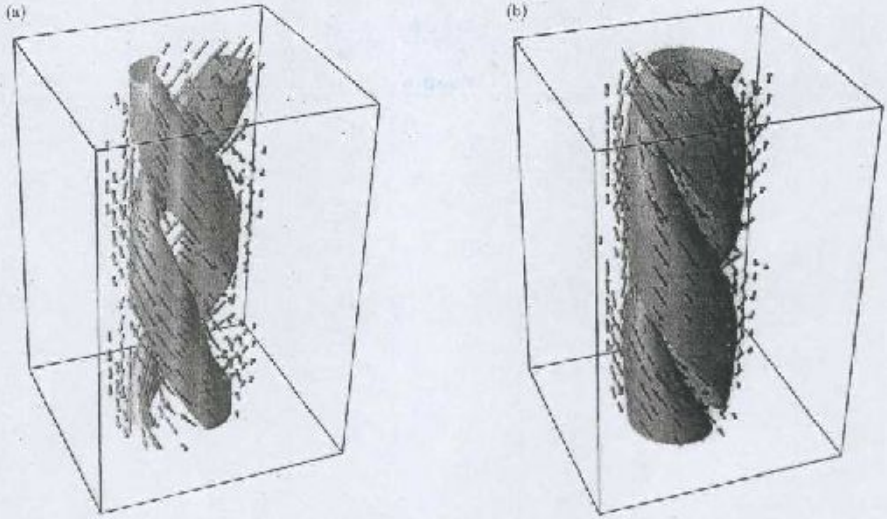

FIG. 5: Three-dimensional representation of the magnetic field in Model 1h. (a) $t = 200$ (end of the kinematic stage); (b) $t = 212$ (the saturated state). Shown are surfaces where $|\mathbf{B}| = 0.05$ of the maximum and magnetic field vectors. The vertical component of the field has opposite sign in the two flux tubes shown (mode $m = 1$). The azimuthal and axial variations of the field are harmonic at the kinematic stage (a) and flattened in the saturated state (b) (see also Fig. 6).

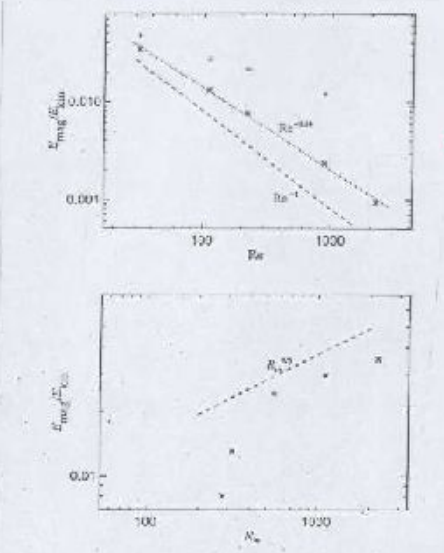

FIG. 11: Magnetic energy in the saturated state versus the kinematic and magnetic Reynolds numbers for Models 1a–i. Top: E_{mag}/E_{kin} as a function of Re for Models 1i, 1a, 1e, 1d, and 1c (asterisks). The crosses refer to a model with volume forcing (see Sect. IV B 3). Bottom: E_{mag}/E_{kin} as a function of R_m for Models 1f, 1a, 1g, 1h, and 1i. The dashed lines show the asymptotic power laws given in Eq. (3); the dotted line is a least square power law fit and corresponds to a dependence $E_{mag} \propto Re^{-0.64}$.

A. Basson A. Gilbert
"Nonlinear equilibration of a dynamo in smooth helical flows"
JFM vol 343 (1997)

The screw dynamo in a time-dependent pipe flow

Wolfgang Dobler
Kiepenheuer Institut für Sonnenphysik, Schöneckstraße 6, D-79104 Freiburg, GERMANY

Peter Frick and Rodion Stepanov
Institute of Continuous Media Mechanics, 1, Korolev, Perm, 614061, RUSSIA
(Dated: January 14, 2003)

FIG. 1: Photograph of a water experiment showing streamlines in an initially spinning torus after abrupt braking. The white object in the channel is the *diverter*, a kind of a fixed ship screw that makes the motion strongly helical. From Ref. [9].

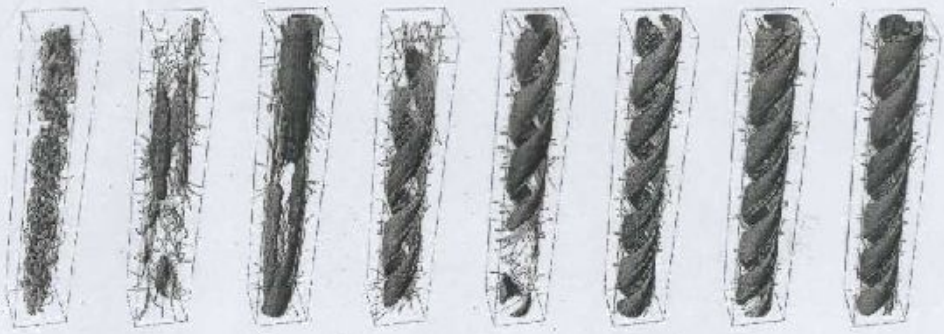

FIG. 9: Structure of the magnetic field for different times of Run 1. From left to right, the times are 0.0, 0.05, 0.1, 0.15, 0.2, 0.3, 0.4 and 0.5 s; the braking time is $T_b = 0.1$ s. The surfaces are isosurfaces of the magnetic field strength (red: $B_z > 0$, blue $B_z < 0$). The lines are magnetic field lines. The diverter is located at the bottom; the direction of the flow is upwards.

G.O Roberts Flow

Roberts. G.O 1970 "Spatially periodic dynamo" Phil. Trans. R. Soc. Lond. 266. 535-558.

Roberts. GO 1972 "Dynamo Action of fluid Motions with two-dimensional periodicity" Phil. Trans. Soc. Lond 271. 411-454.

The flow field we consider is a member of the family of *ABC flows* [4,20,50]

$$\mathbf{u} = (C\sin z + B\cos y, A\sin x + C\cos z, B\sin y + A\cos x). \tag{4.44}$$

These have the *Beltrami property* that $\nabla \times \mathbf{u} = k\mathbf{u}$ for a constant k; here $k = 1$. If $C = 0$ and $A = B = 1$, the flow is independent of z,

$$\mathbf{u} = (\cos y, \sin x, \sin y - \cos x) = (\partial_z\psi, \dot{\psi}, -\partial_x\psi, \dot{\psi}),$$
$$\psi = \sin y + \cos x, \tag{4.45}$$

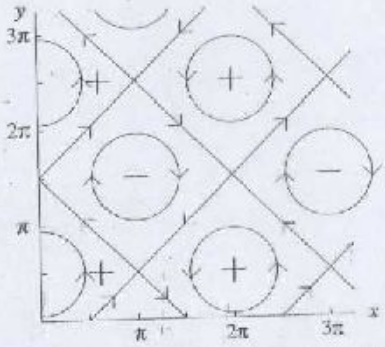

Fig. 3. The G.O. Roberts flow field in (4.45). The + and − signs show the direction of the motion in z, with $u_z = 0$ on the network of separatrices.

9. Numerical results for the four motions

The eigenvalue equations for the four illustrative motions were presented in §8 above, and the symmetry properties of the Fourier components are shown in table 2. The numerical method which was used for finding the eigenvalue p^+ with the largest real part is described in §10 and the accuracy of the programs is defended in appendix C. The results are presented here as curves giving the growth rate,

$$\mathrm{Re}\, p = \mathrm{Re}\, p^+ - \lambda j^2, \tag{9.1}$$

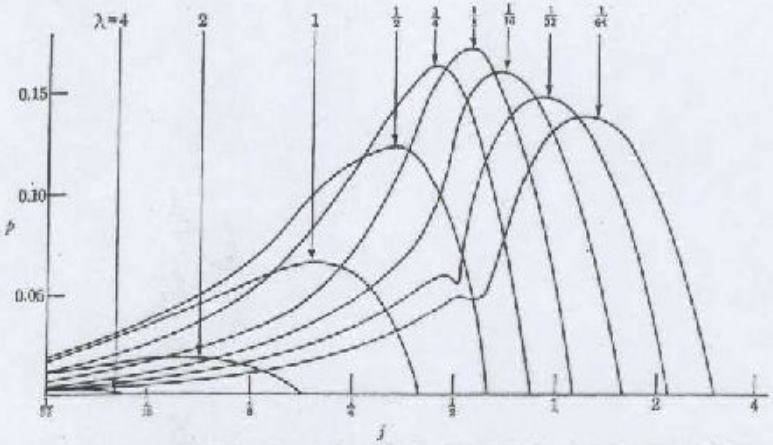

Figure 7. Numerical results giving the growth rate for the first motion for the indicated resistivities λ.

It is first convenient to rotate axes and rescale space, and so write the flow in the form

$$\mathbf{u} = (\sin x \cos y, -\cos x \sin y, \sqrt{2} \sin x \sin y) = (\partial_y \psi, -\partial_x \psi, K\psi), \tag{4.72}$$

with

$$\psi = \sin x \sin y, \qquad K = \sqrt{2}. \tag{4.73}$$

We will solve the induction equation in the dimensionless form

$$\partial_t \mathbf{B} = \nabla \times (\mathbf{u} \times \mathbf{B}) + \varepsilon \nabla^2 \mathbf{B}, \qquad \nabla \cdot \mathbf{B} = 0, \tag{4.74}$$

with $\varepsilon = R^{-1} \ll 1$ now. We note the minor point that the rescaling of space implies a redefinition of the magnetic Reynolds number, and that now $\nabla \times \mathbf{u} = \sqrt{2}\mathbf{u}$. The flow is shown in Figure 4(a).

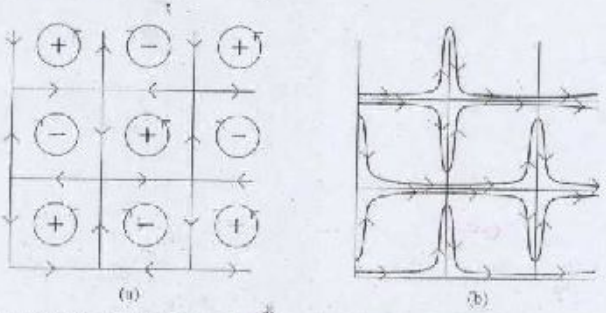

Fig. 4. The G.O. Roberts flow field written in the form (4.72). (a) shows stream lines. (b) shows the steady state with a uniform imposed x directed magnetic field $\bar{b}_x = 1$, $\bar{b}_y = 0$ with $\varepsilon \ll 1$. Magnetic field lines are shown, which are also lines of constant scalar a.

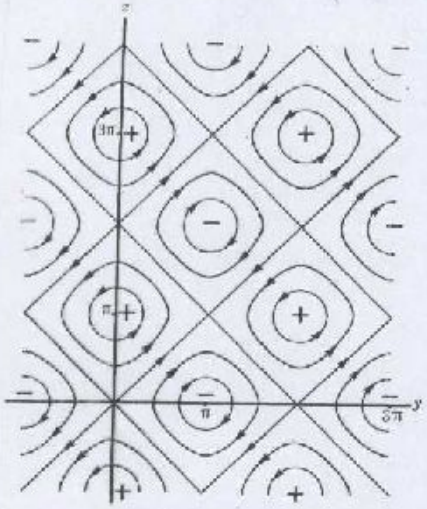

$u = (\cos y - \cos z, \sin z, \sin y).$

$\alpha > 0$

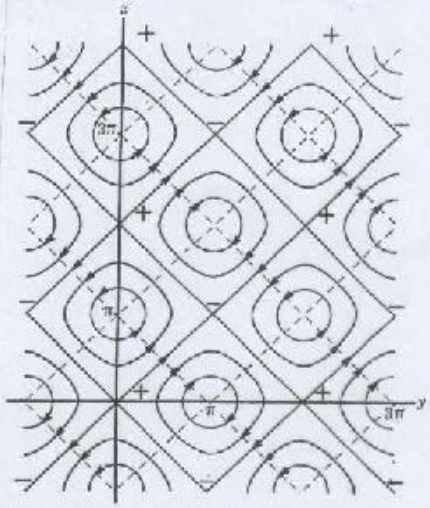

$u = (\cos y + \cos z, \sin z, \sin y),$

$\alpha < 0$

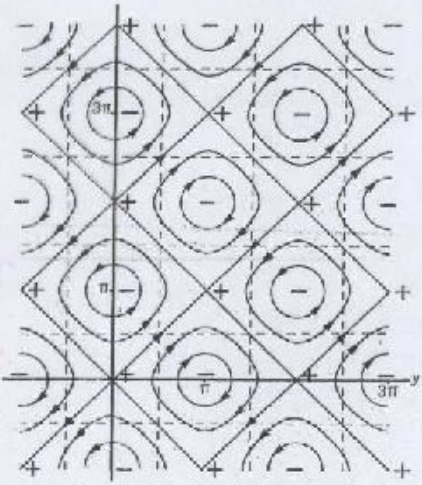

$u = (2\cos y \cos z, \sin z, \sin y).$

$\alpha = 0$

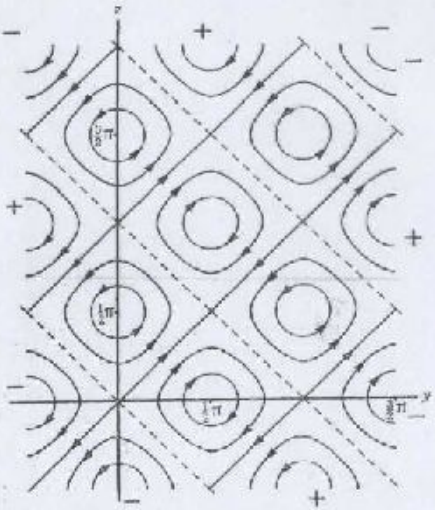

$u = (\sin(y+z), \sin y, \sin z).$

$\alpha = 0$

Subharmonic dynamo action of fluid motion with Two-dimensional periodicity
Proc. R. Soc. Lond. A (1995).

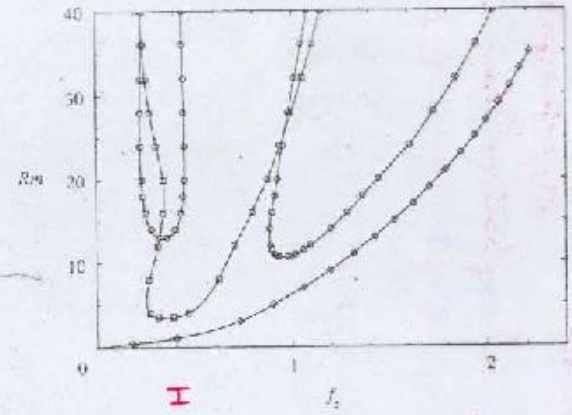

I

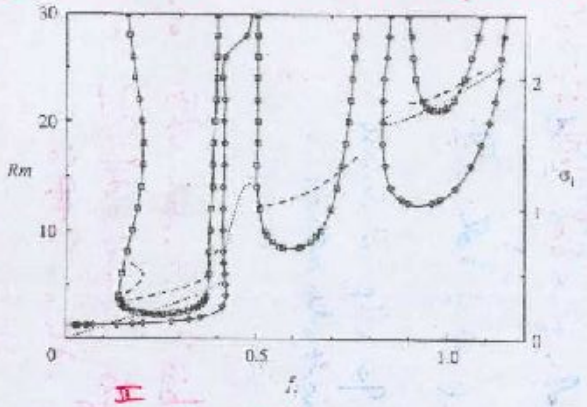

II

Subharmonic case

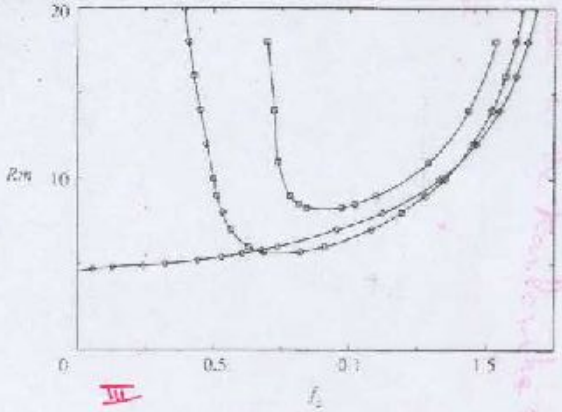

III

Subharmonic

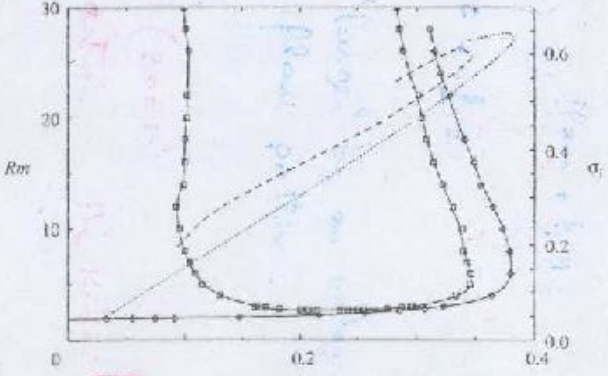

IV

Subharmonic.

"A Kinematic dynamo with a small scale velocity field"
Phys. Lett. A 226 (1997)

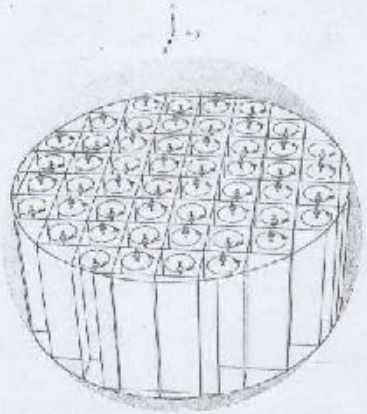

Fig. 1. Sketch of the Childress-Soward flows. A vertical periodic velocity field is contained in a cylinder. The z and x, y components of the velocity are separately indicated. For the simulations, the cylinder is embedded in a spherical volume of fluid at rest (shaded). The figure corresponds to the parameters $A = 1$, $N = 8$ in Eq. (2).

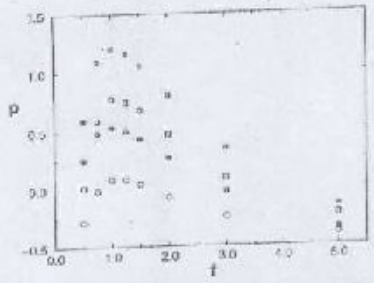

Fig. 3. The growth rate p as a function of f for $A = 1$, $N = 8$. Circles (squares) correspond to $R_m = 20$ ($R_m = 30$). Filled (empty) symbols represent solutions invariant under rotation by 180° about the x (z) axis.

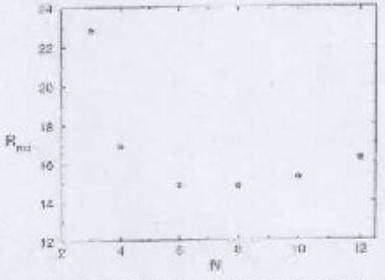

Fig. 4. The critical magnetic Reynolds number R_{mc} as a function of N for $A = 1$, $f = 1$.

Subharmonic case:

$$b = \hat{b}(x, y, f_x, f_y, k)\, e^{i(f_x x + f_y y)}$$

$$B = \mathrm{Re}\left(\hat{b}(x, y, \underline{f})\, e^{(pt + i\underline{f}\cdot\underline{x})} \right)$$

period lengths of B are "larger" by an integer factor N than those flow pattern.

- Plunian. F. Rädler K H (2002)
  "Subharmonic dynamo action in the Robert flow" GAFD, 96.

- Plunian. F Rädler K (2002)
  "Harmonic and subharmonic solutions of the Robert, dynamo model. Application to the Karlsruhe" experiment. magnetohydrodynamics, 38.

C. Nore . M. Brachet, H. Politano and A. Pouquet
physics of Plasmas 4. 71 (1997)

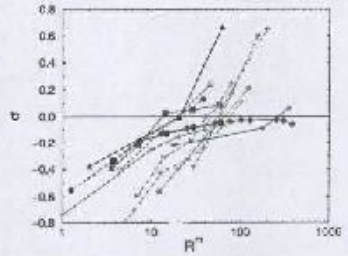

Figure 3: Growth-rates σ of the square magnetic current as a function of $\log R^m$. Symbols for each computation differ according to the type of run: symmetric TG runs with $k_0 = 1$ for $R^v = 14.3$ are represented by circles and solid line, $R^v = 51$ by diamonds and solid line, $R^v = 175$ by stars and solid line; symmetric TG runs with $k_0 = 3$ for $R^v = 12.75$ are represented by crosses and dash line, $R^v = 27.5$ by right triangles and dash line, $R^v = 88$ by stars and dash line, $R^v = 122$ by dots and solid line, $R^v = 153$ by down triangles and solid line, $R^v = 196$ by crosses and alternate dash line; symmetric TG runs with $k_0 = 5$ are for $R^v = 12.6$ (dots and dash line), $R^v = 45.6$ (open dots and dash line); symmetric TG runs with $k_0 = 7$ and $R^v = 20.5$ are represented by up triangles and solid line; and squares and solid line are for the non-symmetric runs with $k_0 = 1$ and $R^v = 14.3$. Growth rates for $< b^2 >$ are identical to those displayed here.

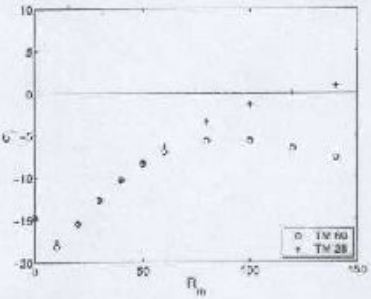

Fig. 5. Energy growth rates σ_r for the most unstable mode ($n = 1$ and $m = 1$) as a function of R_m. Crosses (resp. circles) correspond to the symmetrized velocity field of TM28 (resp. TM60) propeller. The TM28 propeller gives rise to dynamo action for $R_m \simeq 120$ whereas TM60 does not.

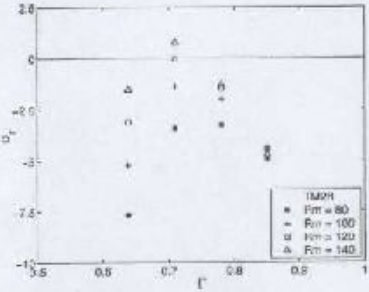

Fig. 6. Energy growth rates σ_r for the mode $n = 1$ and $m = 1$ as a function of the mean poloidal-to-toroidal ratio $\Gamma = U_{pol}/U_{tor}$ for various R_m. The plotted data correspond to the symmetrized TM28 velocity field which as a natural ratio $\Gamma = 0.71$.

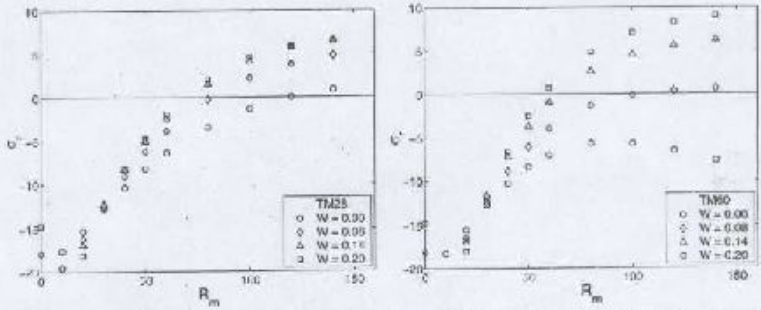

Fig. 7. Conducting layer effects. Maximal growth rate σ_r as a function of R_m for different layer thicknesses $W = (R_{ext}/R_c) - 1$; symmetrized velocity field of propeller (a) TM28 and (b) TM60.

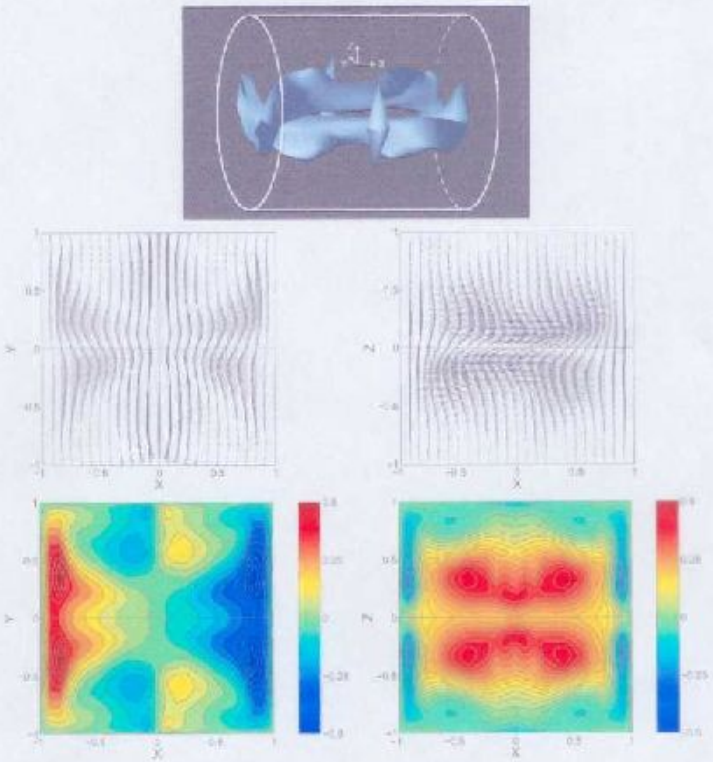

Fig. 8. Self-excited magnetic field of propeller TM28 for $R_m = 140$. (a) Isosurface of the magnetic energy at 50 % of its maximum value in the simulation volume. Poloidal component of the magnetic field in (X,Y) plane (b) and (X,Z) plane (c). (d) Z component of the magnetic field in (X,Y) plane: red (resp. blue) corresponds to vectors pointing out of (resp. into) the plane. (e) Y component in the (X,Z) plane: blue (resp. red) corresponds to vectors pointing out of (resp. into) the plane.

Plane Convection - Driven Hydromagnetic Dynamo.

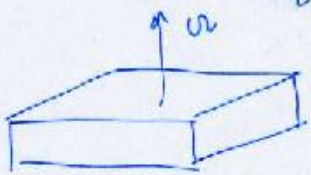

$\Omega \neq 0$
$\Omega = 0$

- S. Childress and A.M Soward (1972) Phys. Rev. lett 29. * 13
  " Convection - Driven Hydromagnetic Dynamo." $\Omega \neq 0$
- F.H Busse (1973) JFM. vol 57. 529-544.
  " Generation of magnetic fields by convection"
- Soward. A (1974) "A convection driven dynamo I the weak fixed case.
  Phil. Trans. R. Soc. lond 275

⋮

Natural forcing for the flow!

Fautelle, Y. Childress (1982) GAFD 22, 235-279
"Convective dynamos with intermediate and strong field." $\Omega \neq 0$

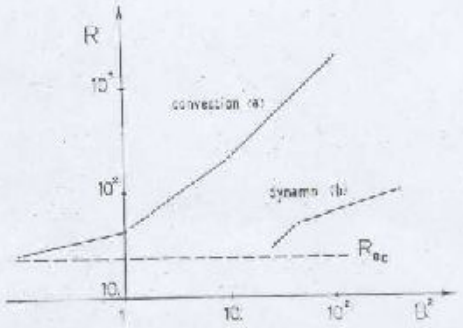

FIGURE 5 The Rayleigh number R is plotted versus B^2, B being a measure of the nondimensional magnetic field; curve (a) is the stability curve; curve (b) corresponds to dynamo solutions.

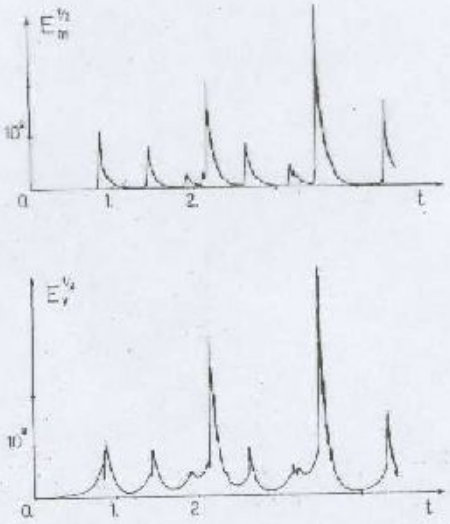

FIGURE 8 Numerical solutions of the modal analysis; the square root of kinetic and magnetic energies are plotted against time (normalized by the magnetic diffusion time scale) for $R = 100$.

Turbulent Dynamos driven by convection.

Run	N	Ra/Ra_c	Pr	Pr_m	Ro	Re	Re_m	Dynamo	E_m/E_u	Re_λ
N1	48	100	1	3	∞	16	50	no	—	12
N2	48	100	1	5	∞	20	100	?	—	18
N3	64	100	1	7	∞	24	170	Yes	3×10^{-4}	15
N4	48	100	1	10	∞	32	320	yes	1.5×10^{-4}	17
N5	48	100	1	7	∞	32	220	yes	3×10^{-4}	20
N6	64	150	1	5	∞	28	140	yes	2×10^{-5}	16
N7	40	150	0.2	3	∞	90	60	yes	2×10^{-4}	10
N8	64	200	0.2	2	∞	100	200	yes	5×10^{-3}	40
N9	64	200	0.2	1	∞	90	90	?	10^{-4}	37
R1	48	150	1	3	0.5	15	45	no	—	10
R2	48	150	1	5	0.5	15	75	yes	5×10.6	10
R3	48	150	1	10	0.5	15	150	yes	10^{-5}	9
R4	40	150	0.2	1	1	45	45	no	—	27
R5	40	150	0.2	2	1	68	90	yes	7×10^{-3}	27
R6	40	150	0.2	3	1	90	115	yes	7×10^{-4}	27

TABLE 1. Identification of the runs reported in this paper. The Rayleigh number Ra is measured in units of the critical Rayleigh number for the onset of convection Ra_c. Pr is the Prandtl number, Pr_m the magnetic Prandtl number, Ro is the Rossby number, Re the Reynolds number based on the integral scale, Re_m the magnetic Reynolds number and Re_λ the Reynolds number based on the Taylor microscale. Note that in the presence of rotation, the dynamo appears more efficient since it can occur at lower Pr_m. The number of Fourier modes is N in the $x-$ and y-directions and $N/2$ in the z-direction.

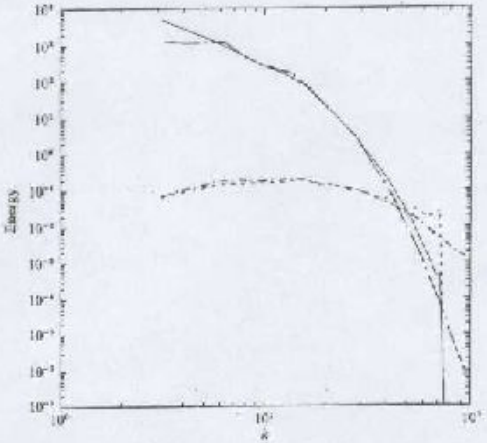

FIGURE 9. Kinetic (solid line) and magnetic (dashed line) energy spectrum at $t = 0.14$. The results of two calculations at different resolution are shown: run N5 ($N = 48$) and run N3 ($N = 64$, curves with inserted dots).

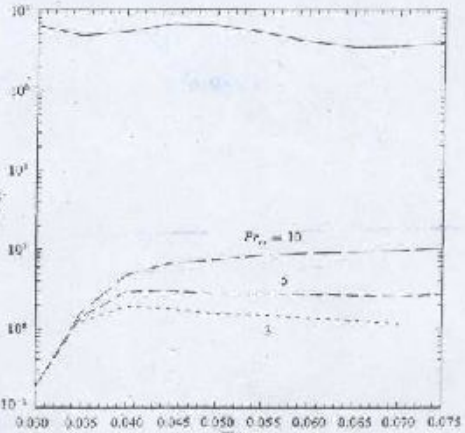

FIGURE 4. Temporal variation of kinetic (solid line) and magnetic (dashed lines) energy for various magnetic Prandtl numbers (indicated on the curves). $Ra/Ra_c = 100$, $Pr = 1$, no rotation.

$\Omega = 0$

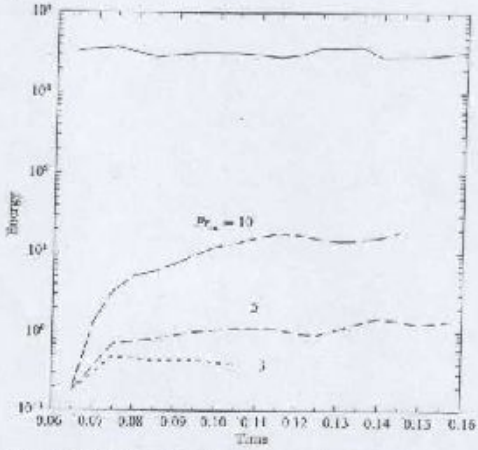

FIGURE 13. Temporal evolution of the kinetic (upper curve) and magnetic (lower curves) energy for various magnetic Prandtl numbers (labelled on the curves) for runs with rotation: $Ra/Ra_c = 12$, $Pr = 1$, $Ro = 0.5$.

$\Omega \neq 0$

. This work remains to be done in three dimensions.

The computational cost of the runs reported here, on a 2 Megawords Cray-XMP, is rather prohibitive. At a resolution of 64^3, it takes 20 hours of CPU time, and twice as much I/O time, to reach $t = 1$ (in units of viscous diffusion times at large scales). Thus we have explored the parameter space letting saturation plateaux establish for moderate times. We have also performed one run at high resolution ($N16$) up to $t = 1$.

Zheligovsky, V.A. & Galloway, D.J. (1998)
"Dynamo action in Chrisotopherson hexagonal flow"
GAFD 88, 277-293

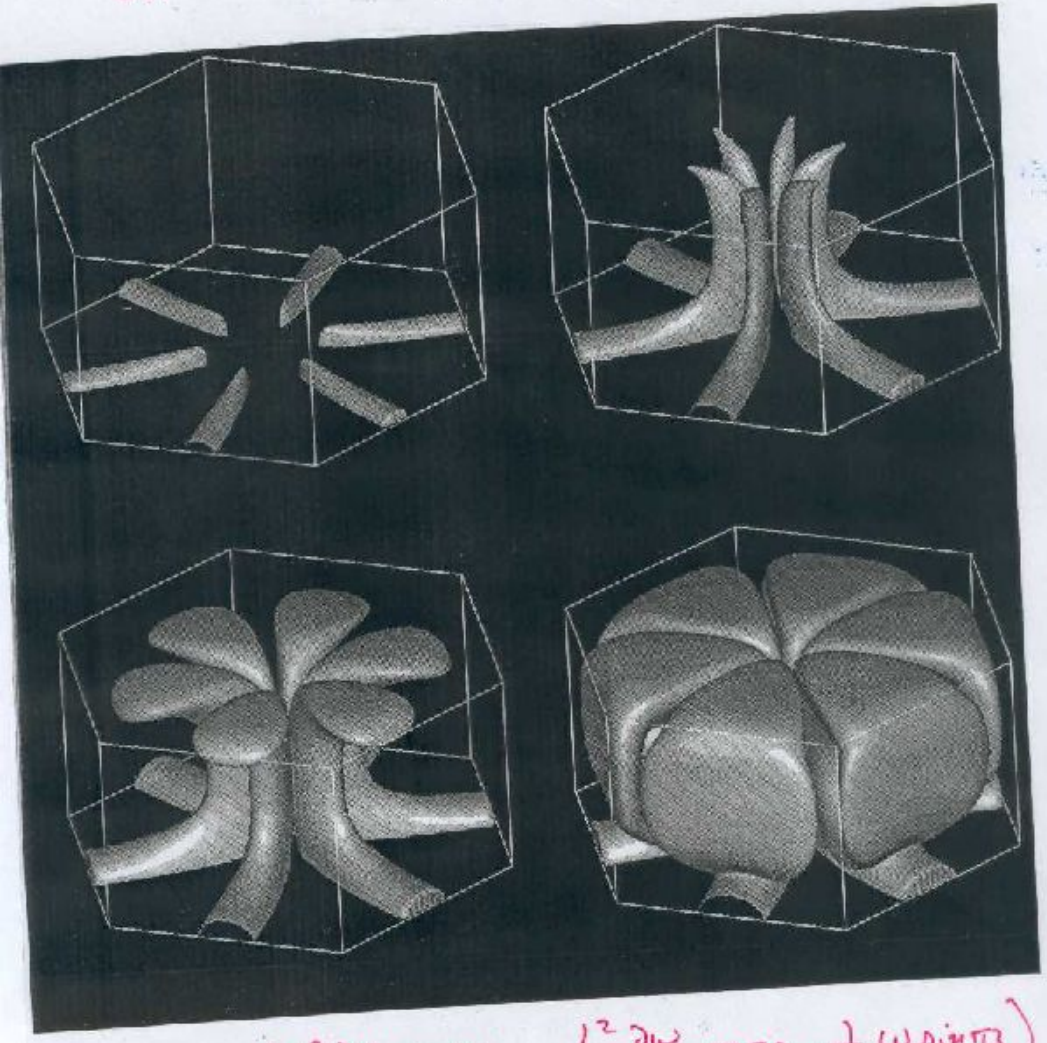

$$V = \left(\frac{L^2}{4\pi} \frac{\partial w}{\partial x} \cos \pi z \,,\; \frac{L^2}{4\pi} \frac{\partial w}{\partial y} \cos \pi z \,,\; \frac{1}{3} w \sin \pi z \right)$$

Figure 3

$$w(x,y) = \cos \frac{2\pi x}{\sqrt{3}L} + 2 \cos \frac{\pi x}{\sqrt{3}L} \cos \frac{\pi}{L}$$

"Dynamo action in simple convective flows"
P.C Matthews.
Proc. R. Soc Lond A (1999)

Convection with rotation

$$u = \begin{cases} \frac{\pi}{k} \sin kx \cos \pi z \\ -\frac{\tau \pi}{k(\pi^2+k^2)} \sin kx \cos \pi z \\ -\cos kx \sin \pi z \end{cases} = \begin{cases} \psi = -\frac{1}{k} \sin kx \sin \pi z \\ v = \frac{\tau \pi}{k(\pi^2+k^2)} \sin kx \cos \pi z \end{cases}$$

electrically perfectly conducting boundaries

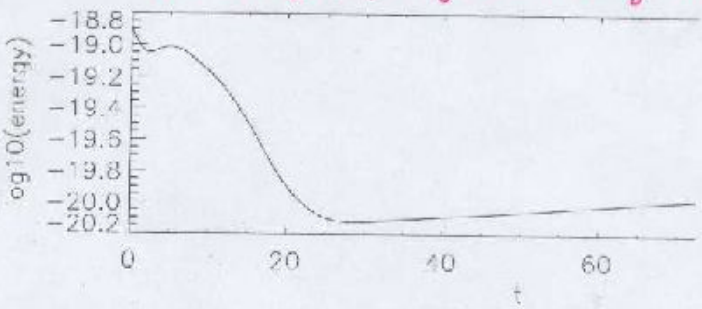

Insulating boundaries conditions

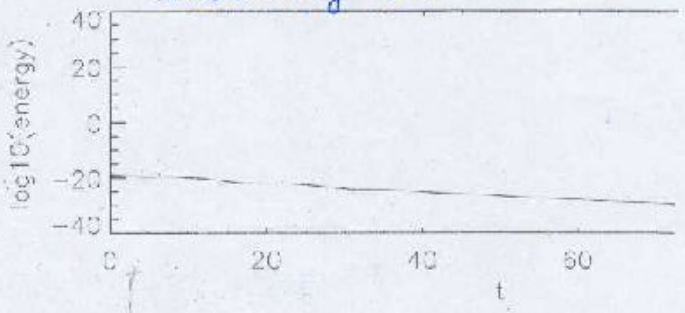

P. C Matthews (1999)

Computed by Y. Park 11 June 2003

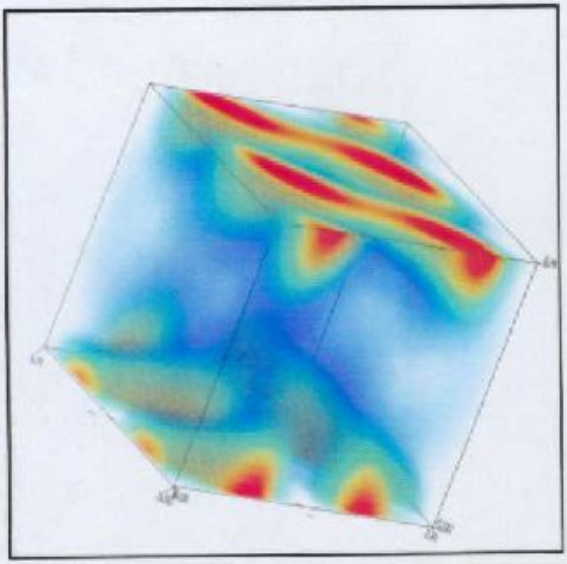

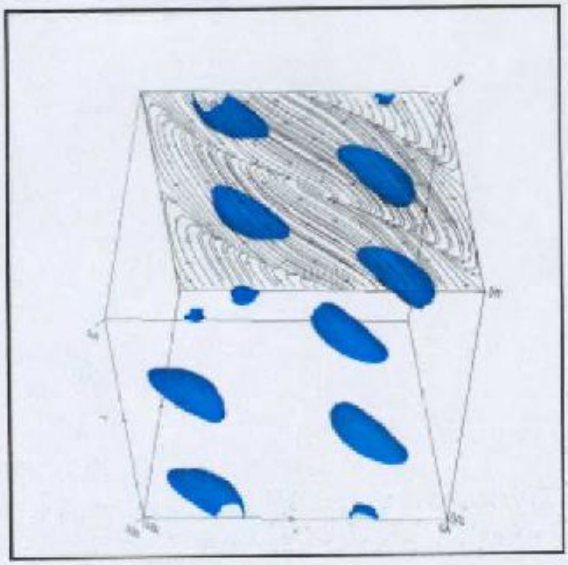

Convection - driven dynamos in a rotating plane layer.
JFM (2000) vol 404.

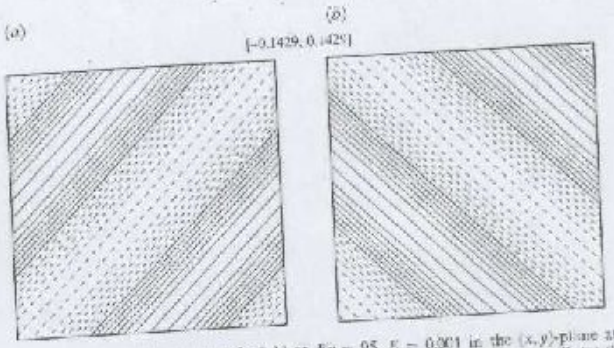

FIGURE 1. Convection without magnetic field at $Ra = 95$, $E = 0.001$ in the (x, y)-plane at $z = 0$ with $\alpha = \beta = 2\pi$. Contours of temperature at intervals of 0.02 for (a) the $(1, -1)$ roll, (b) the $(1, 1)$ roll. In this and subsequent similar figures dashed contours have negative values, the bold contour is the zero level. The values in brackets denote the minimum and maximum values attained by the contoured quantity.

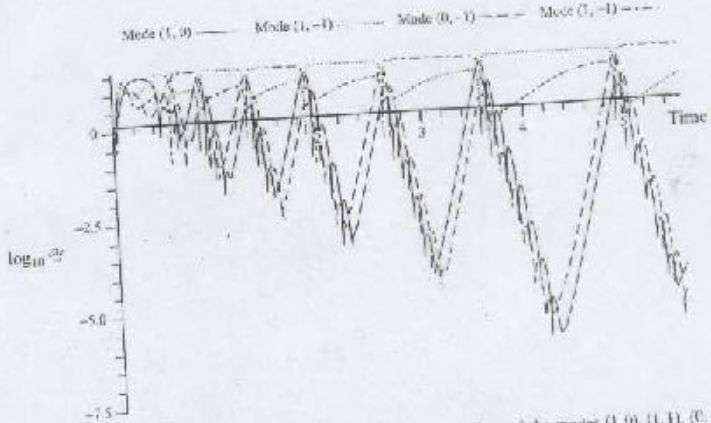

FIGURE 2. The logarithm of the root-mean-square velocity, $\log_{10}\mathscr{E}_{kl}$, of the modes $(1, 0)$, $(1, 1)$, $(0, 1)$ and $(1, -1)$, as a function of time for $Ra = 125$, $E = 0.001$, $\pi = \beta = 2\pi$, showing the heteroclinic cycle.

G. Küppers and D. Lortz "Transition from laminar convection to thermal turbulence in a rotating layer"
J. Fluid Mech 35 (1969)

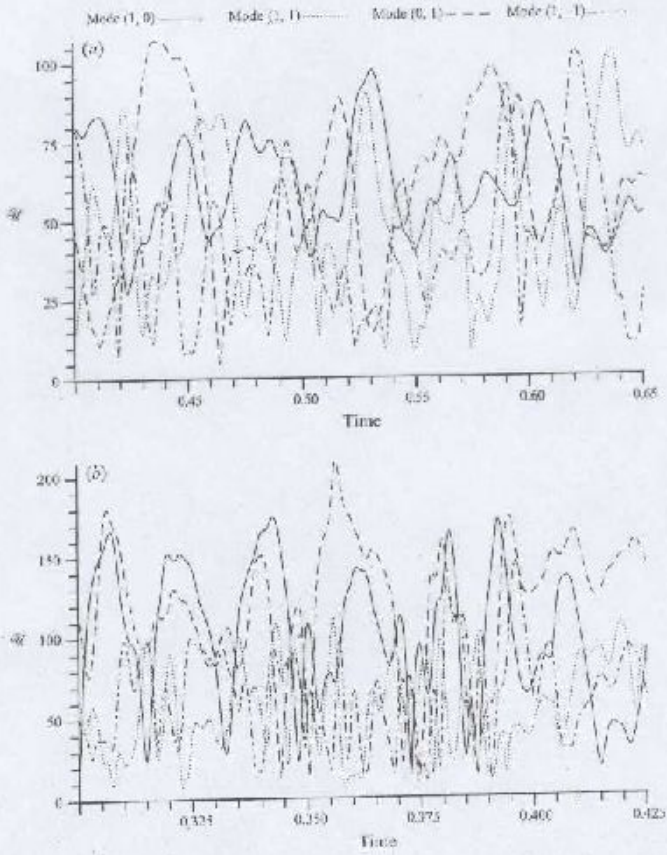

FIGURE 3. As in figure 2 but the amplitudes rather than their logarithms are shown. (a) $Ra = 500$, $E = 0.001$, $\tau = \frac{1}{3} - 2\alpha$; (b) $Ra = 1000$, $E = 0.001$, $\tau = \frac{1}{3} - 2\sqrt{2}\alpha$.

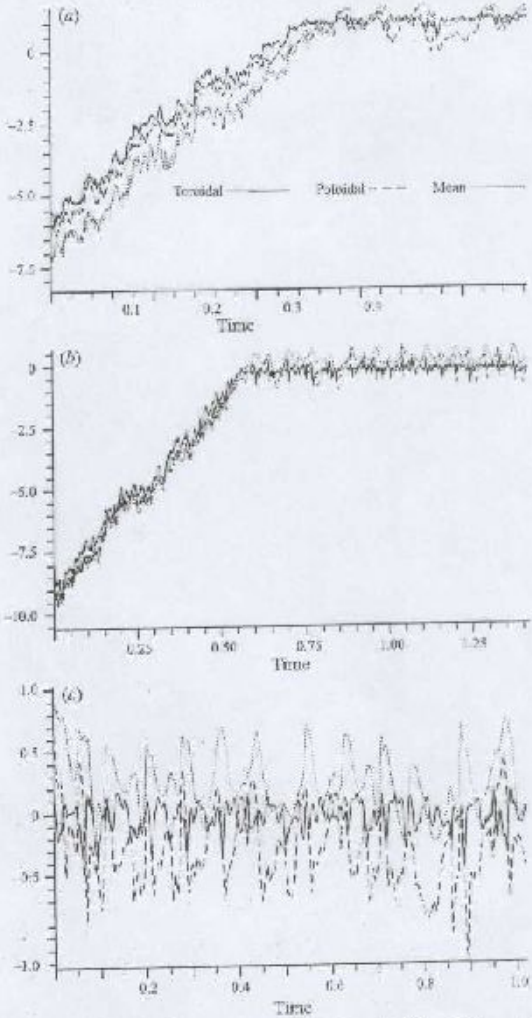

FIGURE 6. Magnetic energy as a function of time for (a) Run A ($Ra = 300$, $q = 5$, $E = 0.00$ $\alpha = \beta = 2\pi$), (b) Run G ($Ra = 1000$, $q = 1$, $E = 0.001$, $\alpha = \beta = 2\sqrt{2}\pi$), (c) Run C ($Ra = 500$, $q = E = 0.001$, $\alpha = \beta = 2\pi$); this case is subcritical only. The toroidal, poloidal and mean field energi $\log_{10}\mathcal{T}$, $\log_{10}\mathcal{P}$ and $\log_{10}\mathcal{M}$, respectively, are plotted.

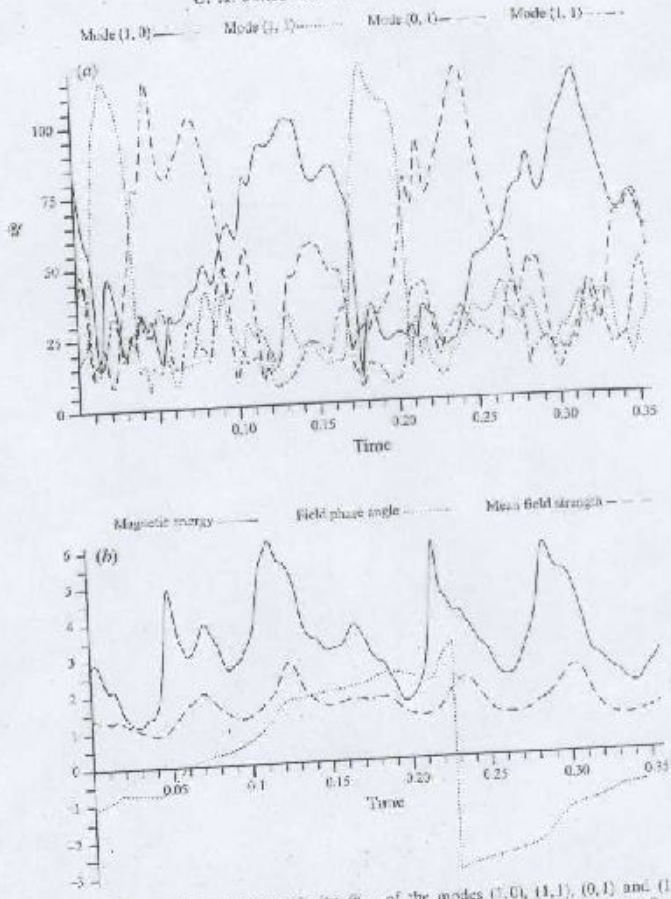

FIGURE 10. (a) The root-mean-square velocity, $\mathscr{R}_m$ of the modes (1, 0), (1, 1), (0, 1) and (1, −1) as a function of time in the saturated cycle for $Ra = 500$, $E = 0.001$, $q = 1$, $\alpha = \beta = 2$. (b) Total magnetic energy $\mathscr{E}_m$, the mean field $(\bar{b}_1^2 + \bar{b}_2^2)^{1/2}$ and the mean field phase angle $\tan^{-1}(\bar{b}_2/\bar{b}_1)$ as functions of time.

J. Rotvig and Chris A. Jones : Phys Rev E 66(2002)

Kinematic dynamo action in large magnetic Reynolds number flow driven by shear and convection
V. Porty, A.D Gilbert, A.M Soward JFM (2001) vol 435

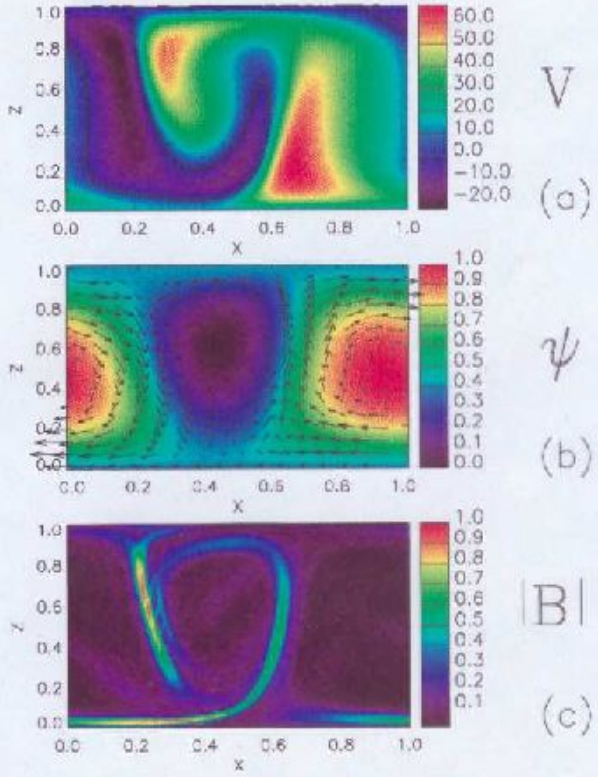

Figure 13: The flow is driven by the rotating convective instability far away from the onset, with the parameter values: $\vartheta = 0°$, $\tau = 120$, $\epsilon = 186.83°$, $Re = 120$, $Ra = 26Rac \sim 1.6\,10^7$ and the Roberts number is taken $Ro = 20 \rightarrow Rm \sim 2280$ with the wave number $k_y = 8.0$. It is shown a time-snapshoot in the (x, z) plane of three different quantities: (a) the total velocity V along the $\hat{y}$-axis (the contour dark line shows the changing sign of V), (b) the total stream function Ψ with an arrow representation of the stream line and (c) the magnitude of magnetic field.

Ekman layer Instability driven Dynamo

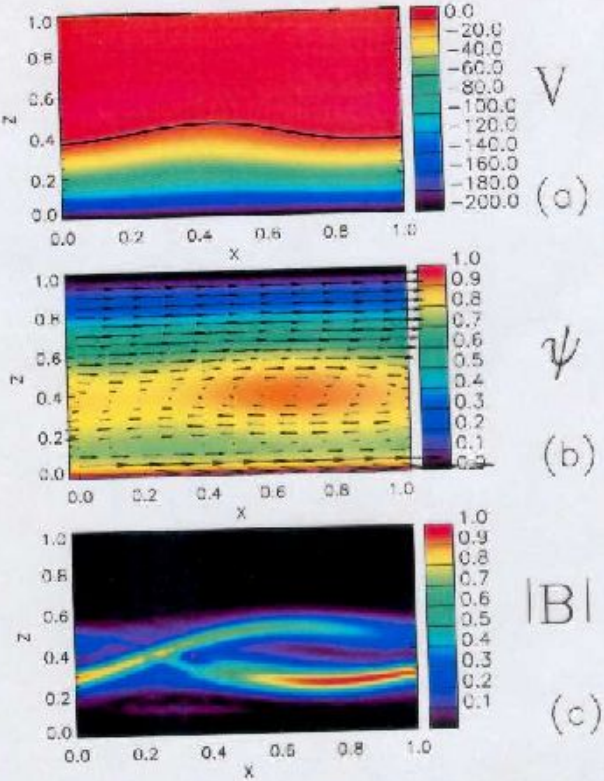

FIGURE 2. A flow resulting from a saturated Ekman layer instability drives a dynamo for $\vartheta = 45°$, $\tau = 60$, $\epsilon = 73.5°$, $k_c = 3.44$, $Re = 210$ and $q = 50$, corresponding to $Rm \simeq 3660$, with the wave number $l = 1.2$. It is shown as a time-snapshot in the (x, z) plane of (a) the total velocity V along the $\hat{y}$-axis (the dark contour line shown as a time-snapshot in the (x, z) plane of (a) the total velocity V along the $\hat{y}$-axis (the dark contour line shows the change in sign of V), (b) the total stream function Ψ with arrows showing the velocity vectors, and (c) the magnitude B of the magnetic field.

A numerical dynamo benchmark

U.R. Christensen [c] J. Aubert [b] P. Cardin [b] E. Dormy [a]
S. Gibbons [d] G.A. Glatzmaier [e] E. Grote [f] Y. Honkura [g]
C. Jones [d] M. Kono [h] M. Matsushima [g] A. Sakuraba [i]
F. Takahashi [g] A. Tilgner [f] J. Wicht [a] K. Zhang [d]

$$E\left(\frac{\partial \mathbf{u}}{\partial t} + \mathbf{u}\cdot\nabla\mathbf{u} - \nabla^2\mathbf{u}\right) + 2\hat{\mathbf{z}}\times\mathbf{u} + \nabla P = Ra\frac{\mathbf{r}}{r_o}T + \frac{1}{Pm}(\nabla\times\mathbf{B})\times\mathbf{B} \quad (1)$$

$$\frac{\partial \mathbf{B}}{\partial t} = \nabla\times(\mathbf{u}\times\mathbf{B}) + \frac{1}{Pm}\nabla^2\mathbf{B} \quad (2)$$

$$\frac{\partial T}{\partial t} + \mathbf{u}\cdot\nabla T = \frac{1}{Pr}\nabla^2 T \quad (3)$$

$$\nabla\cdot\mathbf{u} = 0, \qquad \nabla\cdot\mathbf{B} = 0 \quad (4)$$

In all cases the initial velocity is zero and the initial temperature

$$T = \frac{r_i r_o}{r} - r_i + \frac{210A}{\sqrt{17920\pi}}(1 - 3x^2 + 3x^4 - x^5)\sin^4\theta\cos 4\phi \quad (9)$$

where θ is colatitude, ϕ longitude, and $x = 2r - r_i - r_o$. This describes a conductive state with a perturbation of harmonic degree and order four superimposed. The amplitude is set to $A = 0.1$. In case 1, the initial magnetic field is for $r_i \le r \le r_o$

$$B_r = \frac{5}{8}(8r_o - 6r - 2\frac{r_i^4}{r^3})\cos\theta \quad (10)$$

$$B_\theta = \frac{5}{8}(9r - 8r_o - \frac{r_i^4}{r^3})\sin\theta \quad (11)$$

$$B_\phi = 5\sin(\pi(r - r_i))\sin 2\theta. \quad (12)$$

Results for benchmark case 1

Group	N_r	N_θ	l_{max}	E_{kin}	E_{mag}	T	u_θ	B_z	ω
ACD	48	48	44	30.665	661.913	0.3730	-7.864	-4.779	-3.038
ACD	90	46	44	30.637	623.204	0.3729	-7.669	-4.912	-3.102
ACD	150	46	44	30.732	625.981	0.3730	-7.634	-4.930	-3.105
ACD	200	92	44	30.758	626.284	0.3730	-7.926	-4.933	-3.105
CWG	21	40	28	30.5016	616.085	0.36281	-7.2228	-4.8466	-3.0926
CWG	25	48	32	30.7214	625.872	0.37375	-7.5941	-4.9023	-3.0852
CWG	33	64	42	30.7086	625.413	0.37360	-7.6427	-4.9358	-3.1011
CWG	33	80	53	30.7714	626.406	0.37325	-7.6211	-4.9285	-3.1016
CWG	41	96	64	30.7715	626.416	0.37337	-7.6259	-4.9285	-3.1016
CWG*	49	96	63	30.7715	626.413	0.37337	-7.6235	-4.9284	-3.1016
CWG	65	128	85	30.7734	626.406	0.37338	-7.6230	-4.9289	-3.1017
GJZ	40	36	36(29)	30.1263	617.452	0.36226	-7.0999	-4.8372	-2.992
GJZ	40	52	50(44)	30.5734	622.858	0.37314	-7.6201	-4.9191	-3.083
GJZ	80	52	50(44)	30.7541	625.658	0.37325	-7.6293	-4.9301	-3.100
GJZ	100	54	52(52)	30.7635	626.020	0.37336	-7.6308	-4.9232	-3.101
GJZ	160	78	60(44)	30.7677	626.287	0.37328	-7.6210	-4.9253	-3.101
KS	48	64	42	30.7709	626.434	0.37376	-7.6273	-4.9333	-3.1006
TG	33	64	42	30.7695	626.402	0.37378	-7.6267	-4.9240	-3.0997
TMH	70e		26	31.0259	629.092	0.3679	-7.5823	-4.9226	-3.0949
TMH	70		26	30.7661	627.637	0.3676	-7.6330	-4.9196	-3.0735

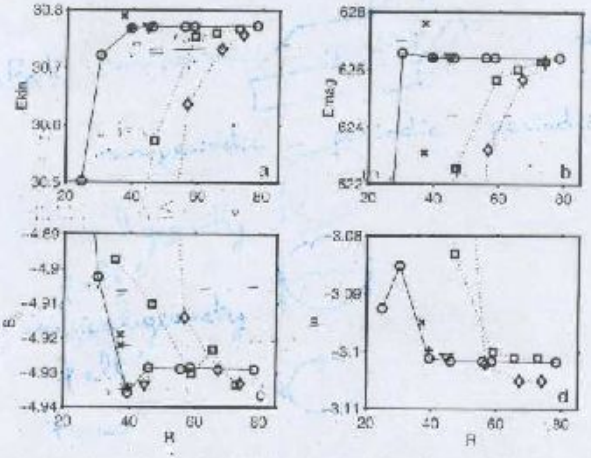

Fig. 3. Convergence of results for case 1. Diamonds = ACD, circles = CWG, squares = GJZ, plus sign = TG, triangle = KS, crosses = TMH (uniform and non-uniform radial grid). a) Kinetic energy, b) magnetic energy, c) local magnetic field component, d) drift frequency.

Table 4
Suggested standard solution with uncertainties

	Case 0	Case 1	Case 2
$E_{\rm kin}$	58.848 ± 0.080	30.739 ± 0.020	42.384 ± 0.045
$E_{\rm mag}$		626.41 ± 3.40	946.80 ± 0.40
$E_{\rm mag}^{\rm ic}$			872.01 ± 1.60
$\tilde{T}$	$3.42812 \pm .00012$	0.27339 ± 0.00040	
u_ρ	-10.1571 ± 3.0020	-7.0260 ± 0.3060	
β_0		-4.9289 ± 0.0090	
ω	$0.1824 \pm .0050$	-3.1017 ± 0.0340	-3.8927 ± 0.0250
$\omega_{\rm c}$			-2.8595 ± 0.0600
Γ_L			-92.970 ± 1.200

Proyt Dynamo Benchmark: 3D

periodic cube

Slab

⇒ convection shear flow

non periodic - periodic - periodic

cylindrical geometry
"full"
"torus"

A new Finite Element Method for magneto-dynamical problems: two-dimensional results

J. L. Guermond [a,1], J. Léorat [b], C. Nore [a,2,*]

Being given source terms, $\mathbf{f}$, $\mathbf{j}$, and initial data, $\mathbf{u}_0$, and $\mathbf{H}_0$, the set of equations is as follows:

$$\begin{cases} \partial_t \mathbf{u} + (\mathbf{u}\cdot\nabla)\mathbf{u} - \nu\Delta\mathbf{u} + \nabla p = (\nabla\times\mathbf{H})\times\mu\mathbf{H} + \mathbf{f} & \text{in } \Omega_c \\ \nabla\cdot\mathbf{u} = 0 & \text{in } \Omega_c \\ \mathbf{u}|_{\partial\Omega} = 0 \\ \mathbf{u}|_{t=0} = \mathbf{u}_0 \end{cases} \tag{1}$$

Fig. 1. Three possible settings for the domain.

$$\begin{cases} \partial_t(\mu\mathbf{H}) = -\nabla\times\mathbf{E} & \text{in } \Omega \\ \nabla\times\mathbf{H} = \sigma(\mathbf{E} + \mathbf{u}\times(\mu\mathbf{H})) + \mathbf{j} & \text{in } \Omega_c \\ \nabla\times\mathbf{H} = 0 & \text{in } \Omega_v \\ \nabla\cdot(\varepsilon\mathbf{E}) = 0 & \text{in } \Omega_v, \\ \mathbf{H}\times\mathbf{n}|_\Gamma = 0, \\ \mathbf{E}\cdot\mathbf{n}|_{\Gamma_v} = 0, \\ \mathbf{H}|_{t=0} = \mathbf{H}_0, \end{cases} \tag{2}$$

where Ω_c denotes the domain occupied by the conducting fluid, Ω_v is the domain of the non-conducting medium, and $\Omega = \Omega_c \cup \Omega_v$ is the total domain. The subscripts c and v stand for conductor and vacuum respectively. To refer to boundary conditions easily, we introduce

$$\Gamma_c = \partial\Omega \cap \partial\Omega_c, \quad \Gamma_v = \partial\Omega \cap \partial\Omega_v, \quad \Sigma = \partial\Omega_c \cap \partial\Omega_v, \quad \Gamma = \partial\Omega = \Gamma_v \cup \Gamma_c \tag{3}$$

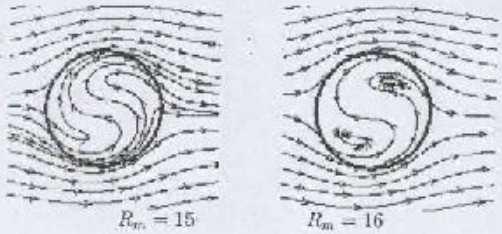

Fig. 2. Streamlines of the magnetic field. First observed reconnections at $\omega t = 4$. Rotation is counter-clockwise.

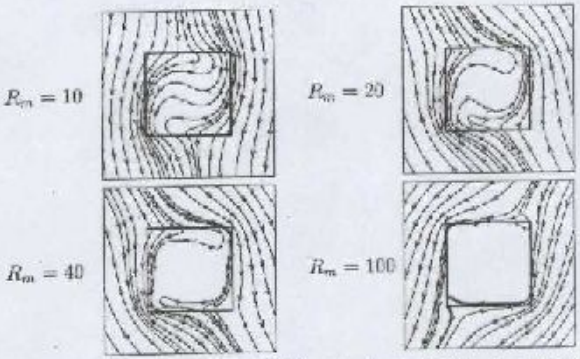

Fig. 9. Streamlines of the magnetic field at steady state. Note the skin effect.

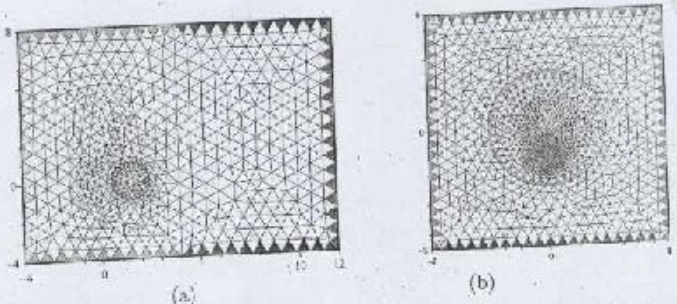

Fig. 22. Integration domains for the semi-infinite sheet (a) and disk case (b). The imposed magnetic field Π_g is limited to an excentred disk of radius $R_i = 1$ centred at $(1.5; 0)$ for (a) and $(0; -2)$ for (b).

Dimitri Laveder : IR (OCA)

AMR Group (NICE MHD Group)

A. Noullez, H. Politano, Y. Ponty.

in contact with.

S. Galtier. IAS

A. Pouquet. NCAR

Hwa - Kardar equation

$$\partial_t u = -u\,\partial_x u + \nu_2\,\partial_{xx} u + \nu_4\,\partial_{yyyy} u$$

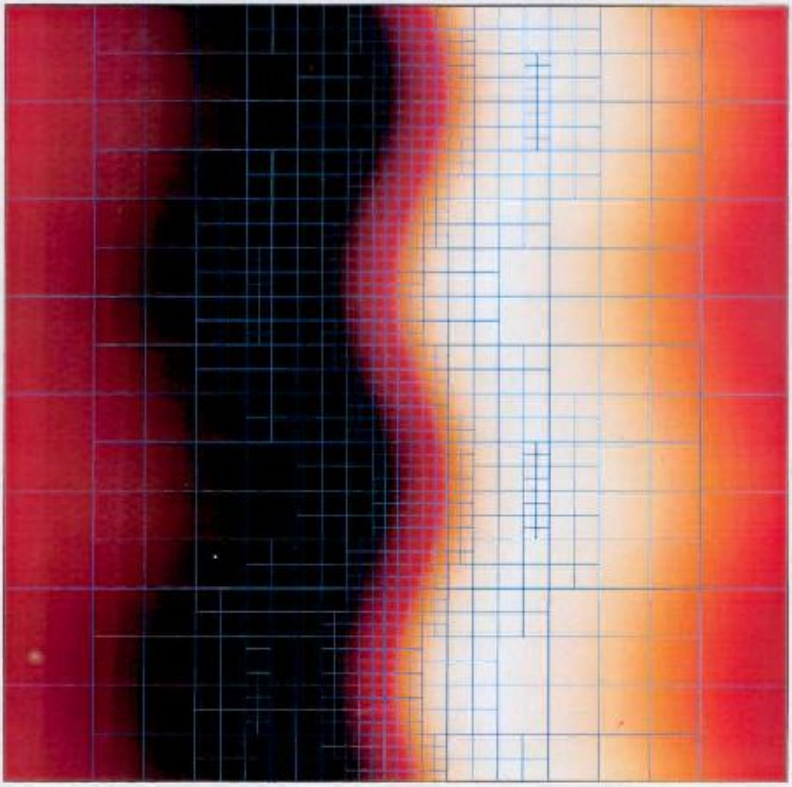

Acknowledgements:

E. Porny

30 bottles of lemon light coke has beem necesary and 2 tabes of skin protector.